Pupil filters in optical systems. Implementation in liquid crystal spatial light modulators

Juan Campos[1], Juan C Escalera[1], Andrés Márquez[2,3], and María J Yzuel[1]

[1]Departamento de Física, Universidad Autónoma de Barcelona, 08193 Bellaterra, Spain;
[2]Depto de Física, Ingeniería de Sistema y Teoría de la Señal, Universidad de Alicante, Ap. 99, E-03080 Alicante, Spain
[3]I U Física Aplicada a las Ciencias y las Tecnologías, Universidad de Alicante, Ap. 99, E-03080, Alicante, Spain

In this paper we review the use of liquid crystal spatial light modulators (LC-SLM) for implementing pupil filters in optical systems. We intend to cover three topics. Firstly, we will study different types of amplitude, phase and complex filters and their effects onto the transverse and axial behavior of an optical system. Secondly, we will describe how to control the amplitude and the phase in an LC-SLM in order to be capable of implementing pupil filters on it. Finally, we will show experimental results of these set-ups improving diverse features of the response of an optical system. © Anita Publications. All rights reserved.

1 Introduction

Pupil filters have been widely used to improve the optical response of an optical system. Non-uniform amplitude-only filters produce effects like apodization or super resolution on the Point Spread Function (PSF) [1]. These types of filters have been applied in very different fields. In other cases, apodizers have been proposed to reduce the effect of aberrations [2-3]. Annular pupils have been widely used to produce lateral super resolution [4]. The use of annular color filters to control the polychromatic response of an optical filter was also proposed [5]. Different super resolution pupils have also been sought through amplitude-only filters in fields like confocal microscopy [6], in some cases combined with polarized light [7] and in microlithography [8-9].

The influence of pupil plane filters in the axial response of an optical system has been investigated [10], and similar filters have been also studied in the polychromatic case [11]. One effect that can be obtained using certain types of filters is high focal depth (DOF) [12]. This property is also interesting in microlithography [13]. It has also been stated that the three-dimensional (3-D) performance of a confocal microscope can be improved [14], where it is especially interesting the use of pupil filters to obtain 3-D superresolution in some applications [15,16]. Pupil filters have been also used to shape a beam, for instance narrow annuli have been used to obtain the so called "diffraction-free" beams [17-19].

Sheppard and Hegedus [10] introduced some performance parameters that describe the focusing properties of rotationally-symmetric pupil filters or masks in the paraxial regime. These factors are expressed simply in terms of the moments of the pupil, and avoid the necessity to calculate the diffracted field of the lens. These gains were generalized in [20] for phase filters, working also near the paraxial plane. Nevertheless, a complex pupil filter can shift the Best Image Plane (BIP) away from the best image plane without filter. So, in [21] we generalized the gain parameters for any complex filter in the surroundings of the shifted focus.

In section 2 we will introduce the calculation of the transverse and axial PSF and the formulation of the performance parameters. In section 3, we will describe some examples of how amplitude only filters can modify the transverse and axial response of an optical filter.

In [22] we studied some conditions that amplitude-only filters must satisfy to produce identical axial response. We showed examples of continuously varying filters, annular binary filters and even annular color filters. In [23] we extended that study to produce identical axial response with a controlled transverse response. We also analyzed those changes which should be introduced in the pupil filter to produce the same

---

Corresponding author :
e-mail: juan.campos@uab.es (Juan Campos)

axial effect when the numerical aperture of the system is increased. By the introduction of a generalized pupil function the results related with the intensity along the axis for low apertures can be extended to high apertures.

In recent years, several works have been centered on the design of phase-only filters [24-29]. These filters may have some advantages over amplitude only filters [24]. Different designs have been proposed to be applied in fields like optical storage or scanning microscopy [24-29]. The main goal of phase filters is to control the 3-D dimensional response of the optical system in order to produce lateral superresolution with a very specific axial response. In some cases high DOF is required [27], but in other ones axial superresolution is needed [28]. Nevertheless, the proposed phase profiles could be very complex limiting their practical applications [25]. For that reason some efforts are done in producing simple phase profiles like annular phase filters [24, 26] or smooth varying phase functions [28]. An extensive study of two-zone and three-zone complex filters can be found in [30-31]. Several symmetry properties of the axial and transverse response that can be useful in the design of complex filters are shown in [32]. Further research of complex filters to produce high focal depth [33] or light sheets has been done [34]. An extensive revision of the use of pupil filters and applications can be found in [35]. In section 4 we will analyze different possibilities of using phase-only and complex filters to improve the impulse response.

Advances in the technology of spatial light modulators (SLM), and particularly in liquid-crystal SLMs (LC-SLM), make possible the implementation of programmable diffractive optical elements (DOE) whose characteristics can be changed dynamically. For these purposes, twisted-nematic LC-SLMs have been especially attractive due to their low-cost and wide availability because of their extensive use as liquid crystal displays (LCD) [36]. LC-SLMs have been used in several applications such as image processing [37,38], diffractive optics [39-40], adaptive optics [41], and in holographic data storage [42]. They have also shown their applicability for the implementation of pupil filters, as we demonstrated both with monochromatic [43-47] and polychromatic illumination [48,49], and both for amplitude filters [43,44,48] and for phase filters [46,47]. In principle, LCDs are designed to be used as display devices [36], where the goal is to show a high intensity contrast. However, in the above-mentioned applications we generally need to work in the amplitude-only regime or in the phase-only regime, i.e. we are mostly interested in the complex amplitude of the wave front instead of its intensity. Therefore, these applications are more demanding on the performance of the LCD than the original display application. Another important point to be introduced is that in general the amplitude and phase modulations provided by a LC-SLM depend strongly on the wavelength used for illumination. This is the main reason why usually LC-SLMs are only applied with monochromatic illumination. However, there are a number of potential applications where it would be very interesting to combine the programmability provided by LC-SLMs and the use of non-monochromatic illumination. In section 5, we will show how LC-SLMs enable to provide the required amplitude and phase modulation, and for monochromatic or polychromatic illumination.

Depending on the design the amplitude filter can produce apodization or hyperresolution in either the transverse plane [1, 50] or along the axis [10, 11]. In [43] we showed how to generate different programmable pupil filters on a LC-SLM working in the amplitude-mostly regime. Among the different DOEs, the lens is likely to be the element that has received more attention. A programmable lens allows changing its focal length without the need of mechanical movement [39, 51, 52]. A very powerful and attractive property of diffractive optical elements is the possibility to combine different functions in the same DOE. It would be very interesting to combine on a single programmable DOE the PSF transformation property of programmable pupil filters with the focusing property of lenses. This combination leads to a new device, so-called programmable amplitude apodized Fresnel lens (PAAFL), whose focal length and whose action on the PSF of the system can both be changed in real time. We demonstrated [44] the feasibility of the PAAFL on a LC-SLM working in the phase-only regime. To display the lens and the amplitude filter in the LC-SLM working in the phase-only regime we extended to a quadratic phase function (in two

dimensions) the method proposed by Davis *et al* [53] to encode amplitude information onto phase-only functions. Furthermore, when displaying the PAAFL, we have to take into account the inherent equivalent apodization effect [54,55]. This phenomenon appears in all focusing DOEs displayed on pixelated devices, such as the LC-SLM. This unwanted phenomenon has to be compensated to obtain the desired response of the optical system. In [56] we demonstrated a technique to measure and to compensate for this effect. In section 6, we review the results obtained for the implementation of amplitude pupil filters on the LC-SLM, and we show how they can be implemented with the device in the amplitude-only and in the phase-only modes, in the latter case it is combined with a diffractive lens.

In an effort to improve light throughput efficiency, different workers have studied the influence of phase only filters in optical systems [30, 31, 57, 58]. In [46] we studied the influence of phase only filters in the pupil of an optical imaging system. The most commonly used merit functions, the point spread function (PSF) and the modulation transfer function (MTF) [59-61], were discussed to make a prediction of the imaging behaviour of the different filters. Since the phase only filters influence both, the image intensity and the position of best image plane along the optical axis it was necessary to analyse the so called 3D-PSF and 3D-MTF. In [46, 47] we selected several types of simple annular phase filters that are easily implemented in SLMs. In some cases, the main goal is to obtain transverse superresolution [24]. The possibility of improving DOF using phase only filters has also been investigated [62]. The increase of the DOF was obtained in [62] in a one step all-optical system, consisting of a lens plus a non-absorptive composite phase mask (CPM), composed of several spatially multiplexed Fresnel lenses. In [63, 64] we proposed and demonstrated a programmable DOE written onto a LC-SLM that is able to provide high DOF. Appropriate lenses with slightly different focal lengths were designed, and these lenses were spatially multiplexed onto the LCD in a random scheme in [64]. In section 7, we show a selection of experimental results dealing with phase-only pupil filters, where images of a sector star object are presented, recorded by implementing different annular phase pupil filters in a LC-SLM. Afterwards, we further analyse how the combination of several diffractive lenses spatially multiplexed in a random scheme onto a LC-SLM enable to increase the DOF of an optical system.

In general, the response of an optical system varies with the wavelength. A typical result is that the optical system may introduce a certain degree of longitudinal chromatic aberration, shifting the BIP for the various wavelengths. In broadband imaging systems these chromatic variations are taken into account in the design process and they are corrected [65]. Even in this case the corrected optical system exhibits, in general, a residual chromatic aberration. Another research field very sensitive to the wavelength of the incident illumination is diffractive optics. For example, in diffractive lenses a change in wavelength produces a change in the focal length and may further produce a change in the diffraction efficiency [66]. As a consequence diffractive singlets are designed and applied for monochromatic illumination. DOEs capability to perform various functions simultaneously may be used to achromatize the performance of diffractive singlets. Different multiplexing schemes exist, such as multifunction coding methods [67, 68], or spatial multiplexing methods [62]. We proposed the use of LC-SLMs with non-monochromatic illumination to generate amplitude apodizers [48] and diffractive lenses [69]. We showed [48] the application of the amplitude apodizers to compensate the longitudinal secondary axial color (LSAC) of a commercial refractive optical system. In this application the LC-SLM is in the amplitude-only regime for polychromatic illumination. In the application to diffractive lenses [69], we demonstrated that we can generate achromatic (i.e. with equal focal length) diffractive singlets valid for a series of discrete wavelengths simultaneously, generated onto the LC-SLM. The LC-SLM is optimized to work in the phase-only regime with polychromatic illumination across the visible spectrum. An appropriate lens for each wavelength was designed, and these lenses were spatially multiplexed onto the LCD. In section 8, we review these polychromatic applications and we show experimental results.

The basic structure of the paper deals with two general blocks. In section 2-4, theoretical and

numerical analysis of the pupil filters is developed. In section 6-8, experimental results are provided using a LC-SLM in a wide variety of configurations and applications based on the previous theoretical analysis. In between, connecting the two blocks, section 5 shows how to generate the required amplitude and/or phase modulation with LC-SLMs. Eventually, in section 9, general conclusions and final remarks are summed up.

2 The calculation of the Point Spread Function with pupil filters. Performance parameters

In the case of a system with radial symmetry the amplitude of the electromagnetic field can be written as [59]:

$$U(v,u) = 2\int_0^1 P(r)J_0(vr)\exp[iur^2/2]\,rdr, \tag{1}$$

with v the coordinate in a transverse plane, u is the coordinate along the axis, r is the radial coordinate in the pupil filter plane, $P(r)$ the filter function placed in the pupil plane, and J_0 the Bessel function of the first kind and zero order.

From Eq (1) we can obtain the distribution along the axial axis by putting, $v = 0$:

$$U(0,u) = 2\int_0^1 P(r)\exp\left[iur^2/2\right]rdr. \tag{2}$$

Following the transformation suggested by Ojeda *et al* [12] we can make the transformation given by

$$t = r^2 + 0.5 \tag{3}$$

The following transformation is also used in many cases [10, 23]:

$$t = r^2. \tag{4}$$

With both transformations (3) and (4) we obtain that the axial amplitude is the Fourier transform of the pupil function $Q(t)$. If we want to study symmetry properties with phase filters [32] it is better to use the transformation (3), and then we can rewrite Eq (2) as:

$$U(0,u) = \int_{-0.5}^{0.5} Q(t)\exp\left[iu\frac{t+0.5}{2}\right]dt, \tag{5}$$

where $Q(t)$ is the filter function $P(r)$ written as a function of t. Then, the intensity along the axial axis can be expressed as:

$$I(0,u) = \left| \int_{-0.5}^{0.5} Q(t)\exp\left[iut/2\right]dt \right|^2. \tag{6}$$

which is the 1-D Fourier transform of the filter function.

Sheppard and Hegedus [10] introduced transverse and axial gain factors describing the focusing properties of rotationally-symmetric pupil filters or masks in the paraxial regime. These factors are expressed simply in terms of the moments of the pupil, and avoid the necessity to calculate the diffracted field of the lens. The treatment holds for real filters, which includes the class of amplitude filters, but also the important class of binary phase-only filters with a phase change of π. De Juana *et al* [20] extended the gain parameters to the case of general phase filters, for the case when the intensity maximum is shifted only a small distance from the geometrical focus. Ledesma *et al* [21] introduced an alternative approach for any complex filter, in which the plane of best focus is calculated first, and generalized gain parameters in the surroundings of the shifted focus are then calculated. We are following below this approach.

In the case of phase filters a high shift of focus may appear. We will calculate the gain factors by considering the shift of focus. Let us suppose that $u_{\max}$ represents the position where the axial intensity has a maximum value. We will expand the expressions for the axial intensity up to second order around $u_{\max}$. The resulting expansion is a quadratic function in $u' = u - u_{\max}$. Then, we will find the values of u' which give a null intensity, i. e. the roots of the parabola, and we will compare these values with those corresponding to the pupil without filter. These points give an idea of the size of the intensity maximum compared to the size that will be obtained for the pupil without filter. The transverse intensity $I(v, u_{\max})$ is also developed up to second order, but now in the coordinate v. The roots of the parabola will be compared with those corresponding with the pupil without filter. We will define the superresolution gains as the ratio between the roots for the pupil without the filter and the roots obtained with filters. When the gain is calculated along the axis it will be called axial gain (G_A), and when it is calculated in the transverse plane we call it transverse gain (G_T). According to this definition, gain values higher than one correspond to intensity distributions that will be narrower than the distribution obtained in the case of the unobstructed pupil. On the contrary, gain values less than one are associated to intensity distributions which are wider than those given for the pupil without filter.

For the axial response we consider a second order expansion of Eq (5) around $u_{\max}$:

$$U(0,u) \cong \exp\left(\frac{iu_{\max}0.5}{2}\right) \int_{-0.5}^{0.5} Q(t)\exp\left[\frac{iu_{\max}t}{2}\right]$$
$$\left\{1+\left[\frac{i\ (t+0.5)}{2}\right](u-u_{\max})-\left[\frac{(t+0.5)^2}{8}\right](u-u_{\max})^2\right\}dt \quad (7)$$

We define the nth moments of the pupil around $u_{\max}$ as:

$$I'_n = \int_{-0.5}^{0.5} Q(t)(t+0.5)^n \exp\left[iu_{\max}t/2\right]dt. \quad (8)$$

Then, Eq (6) can be rewritten as:

$$U(0,u) \cong \exp\left(\frac{iu_{\max}0.5}{2}\right)\left\{I'_0+\frac{I'_1 i}{2}(u-u_{\max})-\frac{I'_2}{8}(u-u_{\max})^2\right\}. \quad (9)$$

As we have mentioned before, in order to calculate the intensity along the axis, we will take into account only the terms up to second order in $u' = u - u_{max}$. In this case the axial intensity approximates to:

$$I(0,u') \cong \left|I'_0\right|^2 - \mathrm{Im}(I'^*_0 I'_1)\,u' + \frac{1}{4}\left[\left|I'_1\right|^2 - \mathrm{Re}(I'_0 I'^*_2)\right]u'^2, \quad (10)$$

where* indicates the conjugate operation.

Equation (10) represents a parabola centered at the point $u_0 = 2\dfrac{\mathrm{Im}(I'_0 I'_1)}{[|I'_1|^2 - \mathrm{Re}\,(I'_0\,I'^*_2)]}$. Note that u_0 is measured from the BIP centered at $u_{\max}$, so its values will be very close to zero for most of the functions that represent axial response of an optical system.

After calculating the roots of the parabola of Eq (10), we can obtain the axial gain as:

$$G_A = 12\frac{\mathrm{Re}(I'_0 I'^*_2)-\left|I'_1\right|^2}{\left|I'_0\right|^2 - \dfrac{1}{2}u_0\,\mathrm{Im}(I'^*_0 I'_1)}. \quad (11)$$

On the other hand, for the transverse response, we evaluate the point spread function at the plane corresponding to $u_{\max}$ and we expand upto second order the transverse response as a function of the transverse

coordinate v in Eq (1). The transverse response can be approximated by:

$$U(v,u_{max}) \cong \int_{-0.5}^{0.5} Q(t) \left[1 - \frac{1}{4} v^2 (t+0.5) \right] \exp(iu_{max}t)dt. \tag{12}$$

Then, the transverse intensity can be expressed as:

$$I(v,u_{max}) \cong |I'_0|^2 - \frac{1}{2} \mathrm{Re}(I'_0 I'^*_1)v^2. \tag{13}$$

As we previously discussed the transverse gain could be defined as:

$$G_T = 2\frac{\mathrm{Re}(I'_0 I'^*_1)}{|I'_0|^2}. \tag{14}$$

In a similar way we can generalize the Strehl ratio. Usually this parameter represents the intensity at the center of the point spread function (PSF) in the focal plane obtained with the filter compared to that obtained with the unitary pupil [10, 20, 21]. The generalized Strehl ratio will be defined as the ratio of the intensity at the center of the PSF in the plane defined by u_0, to the intensity at the center of the PSF for an unobstructed pupil at the focal plane, i.e.:

$$S = |I'_0|^2 - u_0 \mathrm{Im}(I'^*_0 I'_1). \tag{15}$$

For a positive pupil function, G_T can never be greater than two, and it represents a narrow annulus of diameter equal to that of the pupil. $G_T > 1$ means superresolution on the transverse response and $G_A > 1$ means superresolution on the axial response. Amplitude filters produce an axial intensity that is an even function, so the focus always occurs at the origin of u. With phase filters, the focus can be shifted, as we will show later. If G_A is negative, a minimum in the intensity in the axial direction is found at the focal point [10].

For amplitude-only filters it can be also of interest to study two additional parameters. The first one is the energy in the diffraction pattern compared with that in the unobstructed case, given by:

$$E = \int_0^1 Q^2(t)\, dt / (P_{max})^2, \tag{16}$$

the ratio S/E is a measure of the intensity of the focus compared with the total power:

$$F = S/E \tag{17}$$

And finally R represents the fraction of the energy in the central sidelobe (as compared with a plain pupil):

$$R = \frac{S}{G_T E} = \frac{F}{G_T}. \tag{18}$$

Thus S, E, and F are all unity for the unobstructed pupil. It is found that all the properties S, E, F, and R are less than unity for any pupil other than an unobstructed one.

These expressions for the performance parameters, as established in [21], are a good approach for many phase filters, as the intensity peaks on the axis can be situated far from the geometrical focal plane without the filter. The filter is acting like a zone plate. But unfortunately it does not lead to analytic expressions for the filter parameters since numerical calculation of the plane of best focus is needed. For that reason Sheppard *et al* introduced in [70] improved expressions for the gain factors of phase filters, valid for small axial displacements of the true focus from the geometrical focus. The allowed axial displacements are larger than those for the expressions obtained by de Juana *et al* [20]. This method fails completely, however, if an inflection point in axial intensity occurs between the intensity peak and the geometrical focus ($|u_0| > 5$), so that if the intensity peak is distant from the geometrical focal plane, the approach of Ref [21] is necessary. It is interesting to note that Sheppard has extended the expressions for the performance parameters for the high aperture (non-paraxial regime) [71] and for symmetric, cylindrical focusing systems [34].

3 Transverse and axial behavior with transmission only filters

Non-uniform amplitude transmission filters are used in imaging applications to modify the point-spread function (PSF) of an optical system. Depending on the design, the amplitude filter, generically referred as apodizer, can produce apodization or hyperresolution in either the transverse plane or along the axis. We can show that simple polynomial transmission functions can produce these effects. We choose four filters as an example. These filters were studied in the monochromatic case in [10] and in the polychromatic case in [11] and its transmittance is defined by:

filter 1: $P(r) = r^2$; filter 2: $P(r) = 1 - r^2$; filter 3: $P(r) = 4r^2 - 4r^4$;

filter 4: $P(r) = 1 - 4r^2 + 4r^4$ (19)

In Fig 1, we plot the amplitude transmission of these filters.
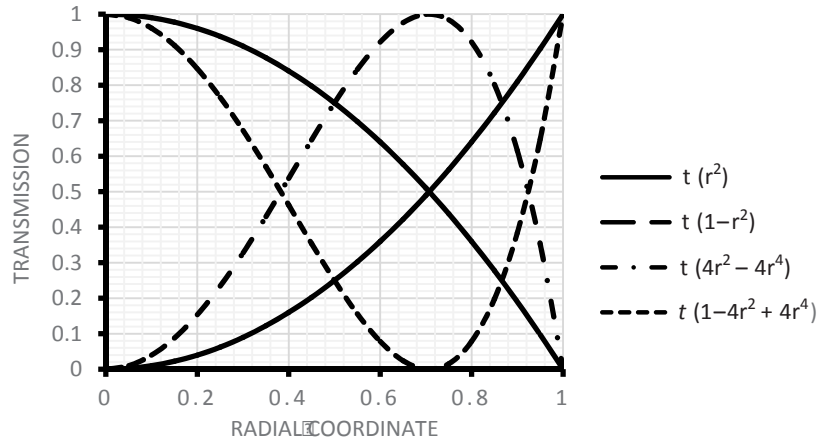
Fig 1. Amplitude transmission of the filters: filter 1, $P(r) = r^2 (-)$; filter 2, $P(r) = 1 - r^2 (--)$; filter 3, $P(r) = 4r^2 - 4r^4 (-\cdot)$; filter 4, $P(r) = 1 - 4r^2 + 4r^4 (--)$.

If we calculate the performance parameters of these filters on the Best Image Plane (BIP) (paraxial plane), we obtain the results presented in Table 1. We have added the annular filter to be compared with filter 1.

Table 1. Performance parameters on the best image plane for the filters: filter 1, $P(r) = r^2(-)$; filter 2, $P(r) = 1 - r^2$ $(--)$; filter 3, $P(r) = 4r^2 - 4r^4 (-\cdot)$; filter 4, $P(r) = 1 - 4r^2 + 4r^4 (--)$ and an annular pupil.

Pupil filter	Transverse gain (G_T)	Axial gain (G_A)	Strehl ratio (S)	Transmitted energy (E)	$F = S/E$
filter 1: $P(r) = r^2$	4/3	2/3	1/4	1/3	3/4
Annular pupil Inner radius $r = 1/3$ Outer radius $r = 1$	5/3	1/9	1/9	1/3	1/3
filter 2: $P(r) = 1 - r^2$	2/3	2/3	1/4	1/3	3/4
filter 3: $P(r) = 4r^2 - 4r^4$	1	3/5	4/9	1/4	5/9
filter 4: $P(r) = 1 - 4r^2 + 4r^4$	1	9/5	1/9	8/15	5/6

According to these results, that are corroborated by the transverse and axial distributions (not shown here), we can summarize the following conclusions:

– Filter 1 [$P(r) = r^2$]: this filter is superresolving (also called hyperresolving) in the transverse direction ($G_T > 1$) and it is apodizing in the axial direction ($G_A < 1$). Please note that it has maximum transmittance in the outer part of the pupil. We call these type of filters *transverse hyperresolving filters.*

– Filter 2 [$P(r) = 1 - r^2$]: this filter is an apodizer in the transverse direction ($G_T < 1$) and it is apodizing in the axial direction ($G_A < 1$). Is axial performance unchanged when compared with that of the previous filter. Note that it has maximum transmittance in the central part of the pupil. We call these type of filters *transverse apodizing filters.*

– Filter 3 [$P(r) = 4r^2 - 4r^4$]: this filter is neutral in the transverse direction ($G_T = 1$) and it is apodizing in the axial direction ($G_A < 1$). It has maximum transmittance for $r = 0.707$, that corresponds to the middle zone of the pupil in coordinate, $s = r^2 = 0.5$ (or $t = r^2 + 0.5 = 1$), this is an important feature, and one of the reasons for using the coordinate changes (4) or (3), respectively. We call these type of filters *axial apodizing filters.*

– Filter 4 [$P(r) = 1 - 4r^2 + 4r^4$]: this filter is neutral in the transverse direction ($G_T = 1$) and it is hyperresolving in the axial direction ($G_A > 1$). It has minimum transmittance for $r = 0.707$, that corresponds to the middle zone of the pupil in coordinate, $s = r^2 = 0.5$ (or $t = r^2 + 0.5 = 1$). We call these type of filters *axial hyperresolving filters.*

One interesting point to discuss is: what are the advantages of using these types of filters? We made a comparison in the polychromatic case in [72]. We will summarize now some conclusions. Firstly, we compared the transverse apodizing filter [filter 2: $P(r) = 1 - r^2$] with equivalent reduced uniform pupils. One strong difference is that uniform pupils do not produce apodization (reduction of the sidelobes), which is interesting for some applications. With equal total transmitted energy, the filter concentrates more energy into the central maximum and the radius of the first minimum is smaller, which is of interest in terms of image quality. The increase in the depth of focus is greater for the binary pupil (although the chromaticity distribution is better for the filter).

Secondly, we studied the different responses between a hyperresolving filter [filter 1: $P(r) = r^2$] and equivalent annular pupils. It is possible to obtain the same hyperresolution with the filter as with annular pupils. However, with equal total transmitted energy, the filter redistributes the energy better into the central maximum (lower sidelobes). The increase in the depth of focus is higher for the annular pupil (although the chromaticity distribution is better for the filter). In Table 1, we can observe that differences comparing filter 1 with an annular pupil that transmits the same energy ($E = 1/3$). The transverse gain is higher for the annular pupil (more superresolution), and the axial gain is lower for it (more depth of focus). Nevertheless, the Strehl ratio and the parameter F is much better for the filter, i.e., it redistributes better the energy to the central peak, and with lower sidelobes.

These types of filters have three drawbacks. The first is inherent to amplitude-only filters: there is a loss of light, as we can observe in the column (E) of Table 1. The second is that it is not so easy to create these type of filters. In section 6, we will show the feasibility of implementing these type of filters in an LC-SLM. The third one is that would be desirable to achieve a desired transverse superresolution or depth of focus choosing certain parameters of the filters. Many studies have been done about this issue, as we discussed in the introduction. In [73] the use of supergaussian rings was proposed. Their amplitude transmission is given by,

$$P(r) = \exp\{-[(r - r_0)/\Omega]^{2\alpha}\}, \tag{20}$$

where r_0 is the center of the supergaussian profile, Ω is the width, and α is the order. For $\alpha = 1$, the amplitude transmittance becomes an annular Gaussian ring. These type of amplitude transmittance contains as particular cases the clear aperture, and the annular window or a ring aperture. We showed that for $r_0 = 0.707$ and varying the parameters α and especially Ω, we can obtain a desired depth of focus at the expense of light throughput.

In a later work [23], we studied general conditions that complex and real valued pupil filters must satisfy to produce identical axial response. When we looked for practical examples, we realized that it was better to modify the supergaussian rings in the variable r to supergaussian rings in variable $t = r^2$:

$$Q(t) = \exp\{-[(t - t_0) / \Omega]^{2\alpha} \tag{21}$$

These pupil functions depend on three parameters. The parameter α determines the shape of the filter, for $\alpha = 1$ the amplitude transmittance becomes an annular Gaussian ring, and for $\alpha \to \infty$ the supergaussian ring is identical with an annular aperture or a ring window. For practical applications we can consider that for $\alpha \geq 5$ the supergaussian ring can be approximated to a ring window (see Fig 2(b)). The parameter Ω controls the width of the ring. α and Ω can modify the value of the transmitted energy (E) of the pupil, especially Ω (see Fig 2(a)). Finally, t_0 is the center of the supergaussian profile (in the variable $t = r^2$) and if the supergaussian ring is not truncated appreciably in the interval [0, 1], the pupil function is symmetrical and then the value of s_0 coincides with the center of gravity of the pupil transmission. According to Eq (14) the transversal gain is $G_T = 2t_0$.
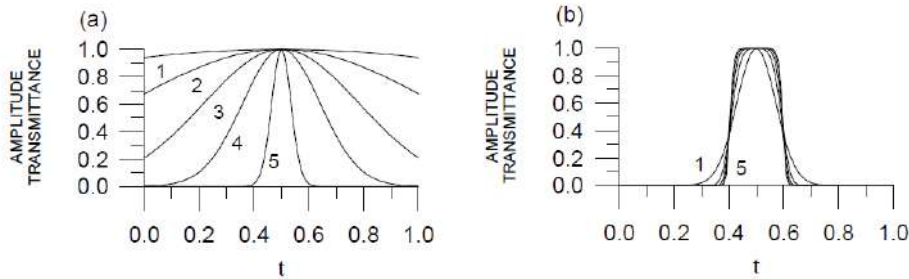
Fig 2. Amplitude transmittance of the supergaussian rings [Eq (20)]. (a) $t_0 = 0.5$, $\alpha = 1$, and (1) $\Omega = 2$, (2) $\Omega = 0.8$, (3) $\Omega = 0.4$, (4) $\Omega = 0.2$, (5) $\Omega = 0.05$. (b) $t_0 = 0.5$, $\Omega = 0.1$, and (1) $\alpha = 1$, (2) $\alpha = 2$, (3) $\alpha = 3$, (4) $\alpha = 4$, (5) $\alpha = 5$.
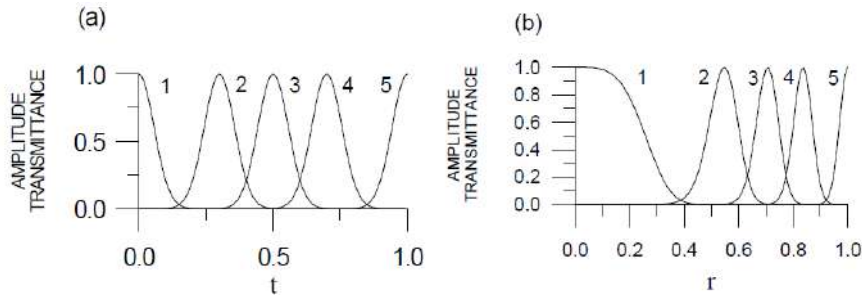
Fig 3. Amplitude transmission of the supergaussian rings [Eq (20)] for $\alpha = 1$, $\Omega = 0.08$, and (1) $t_0 = 0$, (2) $t_0 = 0.3$, (3) $t_0 = 0.5$, (4) $t_0 = 0.7$ and (5) $t_0 = 1$ represented (a) with respect to variable t ($t = r^2$) and (b) variable r.

In [23] we analyzed some practical examples that correspond to pupils with the same axial behavior but with different transverse response.

First, we consider a pupil function $Q(t)$ that presents values different from zero only in a certain interval Δt. Let us now consider a new pupil function $Q(t - a)$ that is equal to the previous pupil function $Q(t)$ but shifted a distance a, in such a way that the new pupil function has not been truncated in the interval [0,1]. Note that to obtain Eq (5) this condition was necessary. Figure 3(a) gives an example, let us assume that curve 3 is the original pupil function, and curves 1, 2, 4 and 5 the same function shifted. The pupil functions represented in curves 2, 3 and 4 fulfill the previous condition, but pupil functions represented in curves 1 and 5 do not because they are truncated. The pupil functions $Q(t - a)$, have the same shape when

they are represented with respect to the variable t (Fig 3(a)) but they do not maintain their shape under this shift when they are represented respect the variable r (Fig 3(b)). Taking into account the translation property of the Fourier transform, the axial amplitude $U(0,u)$ produced by the shifted *pupil* $Q(t - a)$ becomes and then both pupils will produce the same intensity axial response. This result is only valid if the shifted pupil in the t domain $Q(t - a)$ is not truncated in the interval [0,1].

$$U_1(0, u) = \exp(i2\pi\ ua)\ U\ (0, u), \tag{22}$$

Second, let us consider a pupil function $Q_2(t)$ that is obtained by mirror reflection of $Q(t)$ with respect to $t = 0.5$: $Q_2(t) = Q(-t + 1)$. The axial responses of both pupils are related as:

$$U_2(0, u) = \exp(i2\pi\ u)U^*\ (0, u). \tag{23}$$

An example of these pupils are curves 1 and 5 in Fig 3(a). A mirror reflection with respect to another point displaced a distance p can be expressed by $Q_3(t) = Q(-t + 2p)$. This is equivalent to a reflection with respect to $t = 0.5$ and a translation. Then the axial distribution is given by

$$U_3(0, u) = \exp(i2\pi\ u2p)U^*\ (0, u), \tag{24}$$

and then both pupils will produce the same intensity axial response.

Table 2 shows the values of the image parameters G_A, S, E and F defined in section 2 for supergaussian rings in t with values $\alpha = 1$ and $\Omega = 0.08$ and different values of t_0. Some of these pupil filters are represented in Fig 3-a. This figure shows that the supergaussian rings with t_0 between 0.3 and 0.7 are not truncated appreciably, and therefore they present identical axial behaviour. So, they will have identical values of G_A, S, E and F, and this is clearly shown in Table 2. For values of $t_0 = 0.2$ and $t_0 = 0.8$, the truncation of the pupil function is minimal and this is reflected in Table 2, which shows values of G_A, S, E and F very close to the values with $t_0 = 0.5$. For $t_0 = 0.1$ and $t_0 = 0.9$, the difference in the value of these parameters is greater due to the truncation of the function, though even in this case the deviation is smaller than 15%. For $t_0 = 0$ and $t_0 = 1$ (see Fig (3)) the pupil function is in fact a half of that for $t_0 = 0.5$, and consequently the values of G_A, S, E and F are very different. The supergaussian rings with maximum at $t_0 = 0$ and $t_0 = 1$ are examples that fulfil Eq (23) since they are a mirror reflection of each other (see Fig (3)), and they, therefore have identical values of G_A, S, E and F. As we mentioned above, the pupil functions that satisfy Eq (22) have a value of the transversal gain, $G_T = 2t_0$, as shown in Table 2.

Table 2. Supergaussian rings in t, $\alpha = 1$, $\Omega = 0.08$ and different values of t_0.

Supergaussian ring, (t_0)	Transverse gain (G_T)	Axial gain (G_A)	Strehl ratio (S)	Transmitted energy (E)	$F = S/E$
0	0.09	0.0139	0.005	0.0501	0.1
0.1	0.21	0.0322	0.018	0.0996	0.18
0.2	0.4	0.0383	0.02	0.1003	0.2
0.3	0.6	0.0384	0.02	0.1003	0.2
0.4	0.8	0.0384	0.02	0.1003	0.2
0.5	1	0.0384	0.02	0.1003	0.2
0.6	1.2	0.0384	0.02	0.1003	0.2
0.7	1.4	0.0383	0.02	0.1003	0.2
0.8	1.59	0.0383	0.02	0.1003	0.2
0.9	1.79	0.0322	0.018	0.0996	0.18
1	1.91	0.0139	0.005	0.0501	0.1

It must be noted that if the optical system is working with high apertures, some further considerations must be taken into account, as we explain in [23].

We can see that the supergaussian rings in t are very flexible pupil functions (Eq (21)). For values of Ω higher than 2 (see Fig 2(a)), they are very similar to the unobstructed pupil, and for values of Ω lower than 0.1 we can achieve very high depth of focus. The parameter α controls the shape, for values of $\alpha > 5$ they are very close to an annular ring (Fig 2(b)), and for $\alpha = 1$ the shape is a gaussian annular ring. Finally, depending on the value of t_0 we can control the transverse response (superresolution or apodization), being capable of achieving at the same time a desired (to some extent) depth of focus. The main drawback is the loss of energy.

4 Performance of pupil filters with complex transmittance

We have seen in the previous section that amplitude-only filters are capable of improving some features of the impulse response of an optical system, like the resolution or the depth of focus. Unfortunately this is at the expense of light throughput. For that reason many studies have been done in the last years about the use of phase or complex filters to analyse whether similar effects are possible to obtain with less power loss. Filters can be constructed of an array of rings, or alternatively can consist of a continuously variable transmittance.

Now, we will analyze the construction of complex filters made with rings. In particular, the case for the two-zone and three-zone pupil filters (real or complex transmission) were, respectively studied in [30] and [31]. We will summarize some of the results.

Firstly, we consider the simplest example, that of a filter consisting of only two rings, but even this has three independent variables in its design. This filter has received much attention in the past, but here we consider some aspects not described before. Historically, the annular pupil was considered even by Airy [74] and Rayleigh [75] and later by many others [76-78]. The general features of the annular aperture are that the point spread function is sharpened, the Strehl ratio is decreased, the strength of the outer rings is increased, and the depth of focus is increased. Thompson [79] considered structures consisting of a perfectly transmitting outer ring, and a central core of equal area that is partially transmitting, possibly with negative transmittance. An equal area two-ring phase-only filter has been used to control the axial position of the maximum in axial intensity [80]. It has been shown that leaky annular pupils can result in good overall imaging performance [81-82]. More recently, two elements pure phase filters have been discussed [24, 83-86]. However, the general case of a two elements complex filter of arbitrary area ratio has been studied for the first time in [30].

The general problem has three degrees of freedom, the radius of the central zone and the modulus and phase of its transmittance. Even this case is, therefore, quite complicated. We put, $t = r^2$, where t is the radial coordinate normalized by the outer radius of the pupil. We take the boundary between the elements to be at $t = a$, and the amplitude transmittance of the inner and outer elements to be k and 1, respectively. To study the behavior of these pupils we will use the performance parameters we defined in section 2.

We show in [30] that many different designs can be obtained with two rings. We show in Table 3 some interesting results.

One interesting new type of filters is what we call *axially flat* filters. These filters have $G_A = 0$, and they have a very flat axial response. We show in Table 3 two designs that present high superresolution in the transverse response ($G_T > 1.4$). The main disadvantage is that of F and R are not very high, meaning that the sidelobes are high. Sheppard [87] has continued studying these type of filters, improving its behaviour using binary phase filters.

For the other filters in Table 3 we have chosen those that produce moderate transverse superresolution ($G_T = 1.2$), and we have tried improving other parameters.

Table 3. Performance parameters for some two-zone annular pupils.

2 zone Pupil filter	a	k	G_T	G_A	S	E	F	R
2 zone axially flat (AF)	0.2763	−0.3822	1.447	0	0.382	0.764	0.5	0.346
2 zone axially flat-equal area (AF-EA)	0.5	−0.0718	1.577	0	0.215	0.502	0.429	0.272
2 zone equal area (EA)	0.5	0.429	1.2	0.880	0.510	0.592	0.862	0.718
2 zone pure phase (P)	0.0901	−1	1.2	0.552	0.672	1	0.672	0.560
2 zone leaky (L)	0.936	0.190	1.2	1.23	0.0584	0.0973	0.598	0.498
2 zone axially apodizing (AA)	0.214	0.0507	1.2	0.651	0.636	0.787	0.808	0.673
2 zone axially neutral (AN)	0.650	0.441	1.2	1	0.405	0.476	0.850	0.709

− The two-zone equal area filter (EA) minimizes the relative power in the outer rings for a given transverse resolution, as we can see from the high values of *F* and *R*.

− The two-zone pure phase filter (P) maximizes the Strehl ratio for a given transverse resolution, and as it is a pure phase filter there is no loss of light (*E*), the disadvantage is that the values of *F* and *R* are not very high meaning that there are high sidelobes.

− The two-zone leaky (L) has an inner zone of low amplitude transmission, and it minimizes the relative power in the outer rings for a given axial resolution. This design is transverse ($G_T = 1.2$) and axially ($G_A = 1.23$) superresolving (leaky filters). There are potential applications in confocal and multiphoton microscopy.

− The two-zones axially apodizing (AA), that minimizes G_A for a given *F*. That is, it maximizes the focal depth for a given *F*, though it has also quite strong rings in the focal plane.

− The two-zones axially apodizing (AN) is neutral in the axial direction ($G_A = 1$), but it has weak outer rings in the focal plane (R = 0.709).

In general, we have found that for a two-zone filter, there is little advantage in using complex transmittance values. The real filters include those with negative transmittance, including pure phase filters with a phase change of π.

Secondly, we will summarize the results for the three-zone filters. Three zone filters behave differently from two zone filters as a result of the fact that they have an odd rather than even number of zones. The general three zone filter has six independent parameters, as compared with the three of the two zone filter. Three zone filters have been investigated in several papers [82-92]. For a superresolving filter, the point spread function is sharpened, the Strehl ratio is decreased, and the strength of the outer rings is increased. The depth of focus can be either increased or decreased. It has been shown that two or three zone leaky annular pupils can result in good overall imaging performance [81-82]. Here we consider these and other filter designs.

We consider a filter of three elements with real (positive or negative) transmittance in the paraxial, scalar regime. We put $t = r^2$, where *r* is the radial coordinate normalised by the outer radius of the pupil.

We take the boundary between the elements to be at $t = a$ and b, and the amplitude transmittance of the inner and outer elements to be k_1, k_2 and 1, respectively. In this paper [31] we assumed that $|k_{1,2}| \leq 1$.

Table 4. Performance parameters for some three-zone annular pupils.

3 zone Pupil filter	a	b	k_1	k_2	G_T	G_A	S	E	F	R
pure phase symmetrical (PS)	0.458	0.542	1	−1	1	1.2	0.693	1	0.693	0.693
pure phase 3D (P3D)	0.230	0.409	1	−1	1.2	1.2	0.414	1	0.414	0.345
symmetrical leaky (SL)	0.180	0.920	1	0.605	1	1.2	0.558	0.594	0.939	0.939
symmetrical leaky (SL)	0.180	0.920	1	0.284	1	1.5	0.293	0.411	0.713	0.713
equal area transverse (EAT)	0.333	0.667	0.379	0.690	1.2	0.881	0.476	0.540	0.881	0.735
equal area 3D (EA3D)	0.333	0.667	0.503	0.155	1.2	1.2	0.305	0.426	0.718	0.598
leaky optimum 3D (LO3D)	0.111	0.766	0.532	0.322	1.2	1.2	0.254	0.333	0.762	0.635
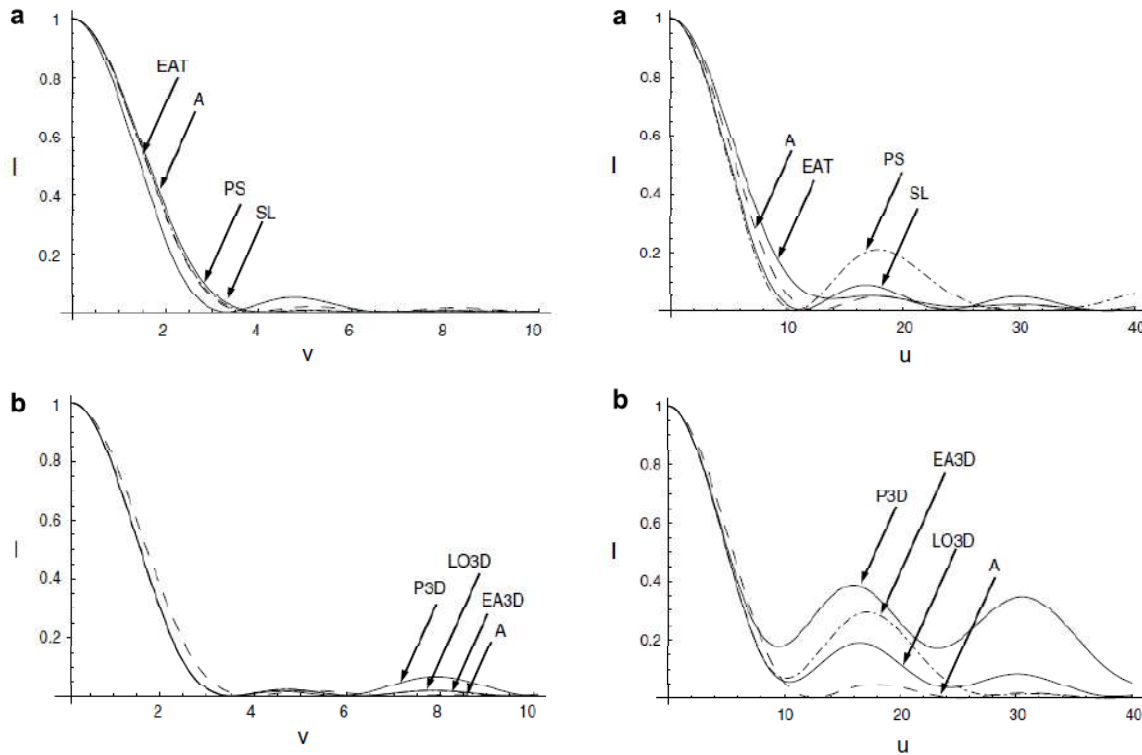
Fig 4. The intensity in the focal plane for the three-zone filters in Table 4 (graphs a and b on the left). The intensity along the optical axis for the three-zone filters in Table 4 (graphs a and b on the right).

The different designs of filter described in this paper are listed in Table 4. The properties of some remarkable two-element filters were given in Table 3. Pure phase filters maximize S. The two zone filter gives the best S for a given G_T, but is axially apodizing. The pure phase symmetrical filter (PS) is axially superresolving, but apodizing in the transverse direction. The pure phase 3D filter (P3D) gives superresolution in 3D with high S. For applications where F is a more important criterion, leaky filters

Juan Campos, Juan C Escalera, Andrés Márquez, and María J Yzuel

give better performance. The symmetrical leaky filter (SL) gives axial superresolution, but is neutral in the transverse direction. Among the filters which produce transverse superresolution, $G_T > 1$, the equal area transverse filter (EAT) gives the best F. For 3D superresolution, the leaky optimum 3D (LO3D) gives the highest F.
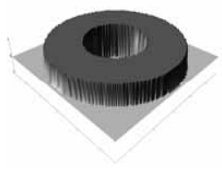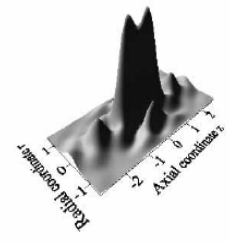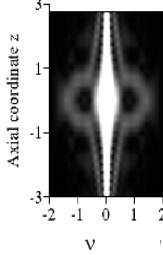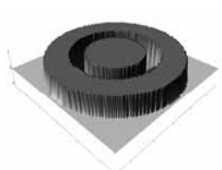
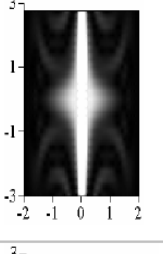Table 5. First column: Phase only filters with different phase values. All the annuli have the same area. Third and fourth columns show the 3D-PSF and the 3D-MTF obtained with these filters.

Filter name	Pupil	3D-PSF	3D-MTF
Without filter			
Filter f1			
Filter f2			
Filter psm			
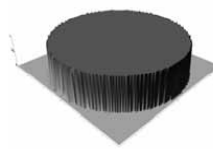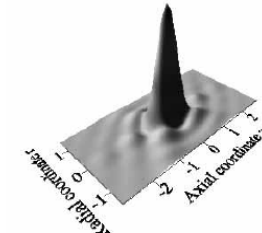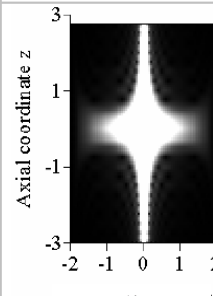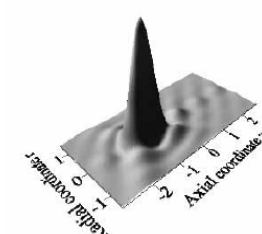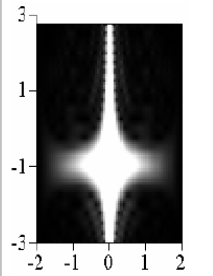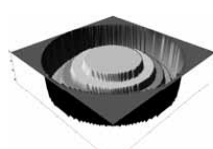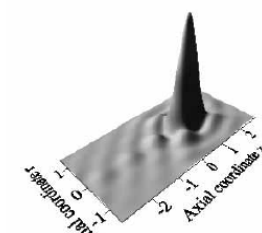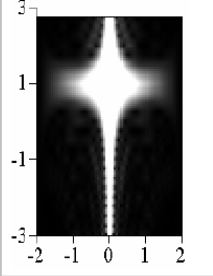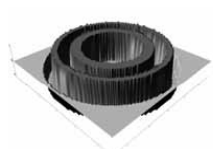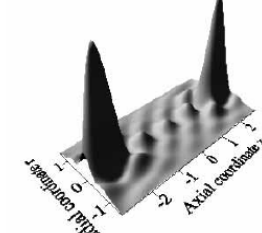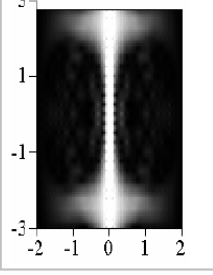
Plots of the intensity in the focal plane and along the axis are shown in Fig 4. Of the filters that give transverse superresolution, we see that EAT gives a stronger first outer ring, and P3D gives a weak first ring, but stronger second ring. LO3D and EA3D both give weak outer rings. P3D, LO3D and EA3D

give increased axial side-lobes. PS and SL both give axial gain with neutral transverse behaviour and weak outer rings, but SL gives stronger axial side-lobes.

Table 6. First column: Phase only filters which are represented by one annulus that causes a phase shift of π located in different positions. Third and fourth columns show the 3D-PSF and the 3D-MTF obtained with these filters.

Filter name	Pupil	3D-PSF	3D-MTF
Filter p1			
Filter p2			
Filter p3			
Filter p4			
Filter p5			
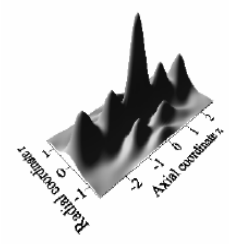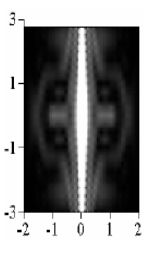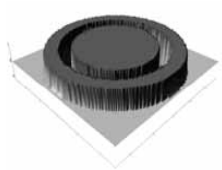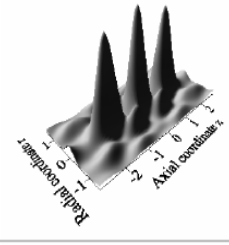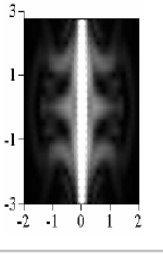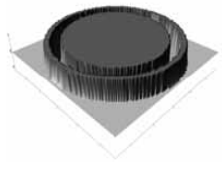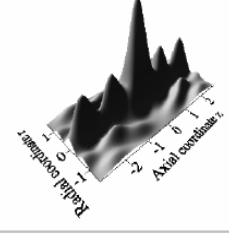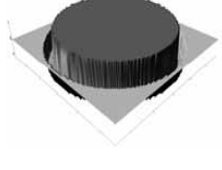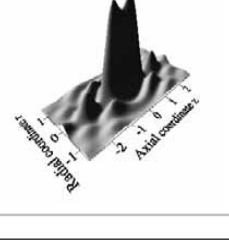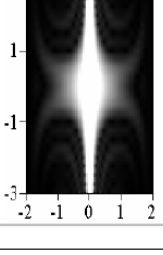
In general, the performance of the three-zone filters is superior to that of the two-zone filters [30]. LO3D, PS and SL are all interesting and potentially useful designs of filter.

We have continued our research work with phase annular filters in [46-47]. First, the phase only filter under discussion was divided in five equally area annuli. The phase variations are either linearly increasing or decreasing with the annulus number or alternating between 0 and π. Second we have used a filter that consists on one phase annulus with a phase shift of π in different positions over the pupil.

The phase only filters under discussion consist of five annuli of equal area. The phase value of each annulus is constant, and it can be different in each annulus [46-47]. The different filters under discussion are summarized in Tables 5 and 6. The filters should not realize any absorption within the pupil. The optical system is aberration free and the size of the pupil is normalized to one.

The filters given in Table 5 show a linear increasing (f_1) or decreasing (f_2) phase function. Because of the condition of equal-area annuli the phase function can be approximated by a polynomial (quadratic) phase-function, instead of a linear step function. That's why one can expect that the filters behave like additional lenses, since the transfer function of a lens in the pupil plane is described by a quadratic phase function in the Fourier theory of optical image processing [60, 61] as well. The filter (psm) is a binary phase filter with an oscillating phase value that produces two foci.

The other group of studied phase only filters is given in Table 6. This table includes phase only filters, where the phase influence is caused by a phase shift of π in different positions. This type of filter causes a change of the sign of the wavefront in the region of the phase shift.

The third column of Table 5 shows the calculated 3D-PSF. The radial and the axial behaviour of the PSF of the filters f_1, f_2 and psm is described. The results are compared with the diffraction limited pupil without any filter. The filters under consideration cause a shift of the best image plane that can be observed in Table 5. Filters f_1 and f_2 are an approximation of a lens made with five phase levels. This explains the effect of these filters shifting the best image plane. The fact that we are using only five levels produces a decrease in the light efficiency and consequently the maximum intensity is slightly lower with these filters than with the clear pupil. It can be shown [33] that the amplitude distribution along the axis is the Fourier Transform of the pupil function expressed in r^2. In these conditions the filter psm is like a grating that produces different orders. In Table 5 the +1 and −1 orders can be observed, which produces multifocal planes.

The 3D-PSFs for the different annulus are shown in Table 6. Compared with the case without filter, the PSF with the annulus phase filters show strong side lobes. Looking at the 3D-PSF for filters p1 and p5, the value along the axis are equal, this is the same if one considers the graphs for filters p2 and p4. However, the transverse PSF's are different, as we have already shown [46]. These results can be explained by expressing the pupil in terms of r^2 [33]. With this coordinate change filter p1 is the symmetric to filter p5 and the same happens with filters p2 and p4. It was shown [33] that these filters should produce the same axial behaviour but different transversal response. In the transverse plane, if one filter is apodizing its symmetric one is hyperresolving.

Some differences appear in the radial PSF. Filter p5 shows no side lobes and the extension of the function in the region of the first minimum is the widest. So filter p5 behaves like an apodizing filter [13, 93-94]. High spatial frequencies are suppressed, that means sharp edges are smoothed and the resolution is lower. On the other hand filter p1 has a narrow PSF and a high first maximum, so one can conclude that this type of filter is "hyperresolving" [13, 93-94]. The edges of an imaged object are improved; the resolution is improved as well. The same conclusions can be done for filter p2 and p4. All these results confirm the symmetry properties of filters p1, p5 and p2, p4.

The 3D-MTF [47] is depicted in the last column in Table 5. The MTF of the diffraction limited pupil is regarded to estimate the 3D-MTF of the filters. The contrast of the high spatial frequencies decreases with the defocus rapidly. In some frequency regions we have a contrast inversion. One can see that the filters

f_1 and f_2 cause a shift of the best image plane. The best image plane corresponds to the plane where the MTF is wider. The filter psm produces two images with a high contrast in two symmetrical positions with respect to $u = 0$. Compared with the empty pupil the contrast of the high spatial frequencies is decreased.

The MTF for the filters described in Table 6 shows a strong decrease of the contrast for all of them. In general the greatest decrease for low frequencies is caused by the filter with the phase shifting annulus at the outer position. The contrast in the middle region of the spatial frequencies increases if the phase shifting annulus is shifted from the inner to the outside regions. Moreover, the best contrast for high spatial frequencies (small grating periods) corresponds to filter p1. In the best image plane ($u = 0$) filter p5 produces a contrast decrease in the higher frequencies in comparison with the clear pupil, but the contrast is maintained along the axis for a longer distance. This means that we will have an effective increase of the depth of focus.

Filter p3 produces three planes with a high contrast for intermediate/high frequencies that are located at $u = \pm 1.5$, and $u = 0$. These planes correspond to the focalization planes. Filter p1 shows a very high contrast in the best image plane ($u = 0$) in the low frequency range. The intermediate frequency range is almost lost and the contrast increases in the higher frequencies. Experimental results for these filters implemented in a SLM will be shown in section 6.

We have seen before that there is an increasing interest in using phase pupil functions which are easier to be produced to obtain high focal depth [19, 32]. In some cases annular phase filters have been proposed [30-31], in other cases continuously varying phase filters are used [20-21]. In [32] we showed several symmetry properties which may help to design pupil phase filters.

It has been shown that amplitude [43-44] or phase filters [40] may be implemented in spatial light modulators. In [48] it has been reported the use of a programmable apodizer to optimize the chromatic aberration effects using a liquid crystal spatial light modulator working with polychromatic light.

In [63] a complex filter was proposed, consisting of an external ring where two portions of lenses are multiplexed. One of the lenses is a convergent one and the other is a divergent one. The effect of this combination is to shift the focus in front of and behind the best image plane (BIP), defined for the pupil without filter. With this filter we obtain a high focal depth and transverse superresolution along the extended focus.

As we have mentioned, another point to be considered in the pupil design, is the transverse superresolving effect. Different positions of the centre of the combined ring could give different transverse responses and the same axial response. As we have discussed in [32] a pupil with real transmission will act as transverse apodizing filters if the centre of mass is located in the $t < 0$ (being $t = r^2$) region and as transverse superresolving filter if it is located in the $t > 0$ region. For complex pupils, it is not easy to predict the behaviour of the pupil and the transverse gain must be calculated for each particular case.

In our case, we have verified that if the combined pupil function occupies the external portion of the clear aperture, then the transverse response is superresolving along all the extended focus. Additionally, a better illumination condition is obtained if a large area in the clear aperture is used. By taking into account these considerations, we have selected a combined pupil function that can be described by

$$Q(t) \quad \begin{cases} 0 & 0 < t \leq 0.5 \\ e^{i4.4\pi t} & 0.5 < t \leq 0.75, \\ e^{i(-4.4\pi t + 2.2\pi)} & 0.75 < t \leq 1. \end{cases} \tag{25}$$

In Fig 5(a) we show the axial response produced by this pupil function where an excellent DOF can be appreciated. We can estimate the depth of focus as the full width at half maximum (FWHM). By calculating the ratio of this parameter for this pupil function and for the clear pupil system we obtain a factor of approximately eight.

We have studied the transverse response in planes along the interval where we define the FWHM, to be sure that super resolution is obtained in the extended focus. As an example, we show in Fig 5(b) the transverse response at coordinates $u = -30$, $u = 0$ and $u = 30$ along the axial axis. It can be observed that the transverse intensity is almost the same in these three planes and we have always a super resolving effect.
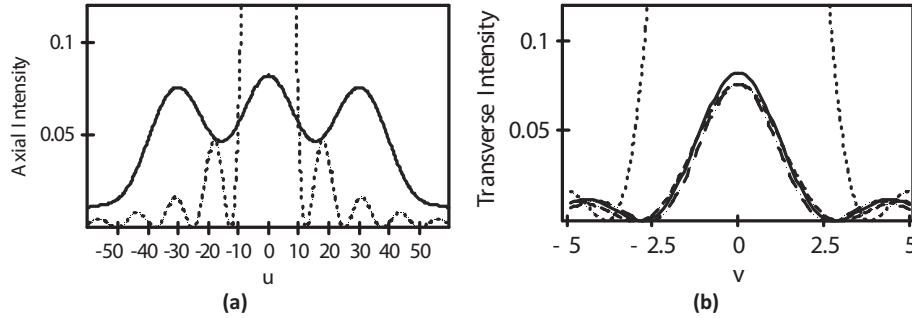

Fig 5. Responses of the annular pupil described by Eq (25): (a) axial distribution and (b) transverse intensity obtained at, $u = -30$ (dashed line), $u = 0$ (fill line) and $u = 30$ (dashed – dotted line). In dotted line the response for the clear aperture.

In Fig 6 we show the evolution of the transverse gain defined along the axis. The transverse gain factor is always higher than one, which guarantees a superresolving effect for every transverse plane.
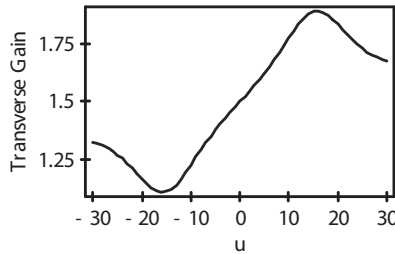

Fig 6. Transverse gain factor of the annular multiplexed filter of Eq (25) as a function of the axial coordinate.

So, in summary, we see that the proposed pupil function has a complex transmission that produces a high depth of focus and transverse superresolution. The proposal consists in adding two quadratic phases in two annular region of the pupil. One of the quadratic phases corresponds to a convergent lens while the other corresponds to a divergent lens. These lenses have the effect of shifting the light in front of and behind the BIP corresponding to the system without filter. These shifts have been selected to have an extended DOF. With the position of the annuli, the transverse gain can be controlled. We have chosen the position of the filter in the outer part of the pupil in order to improve the transverse resolution in comparison with the system without filter.

In other works we have followed similar strategies to increase the depth of focus. In [64] it was proposed a combination of several diffractive lenses written onto a single programmable liquid crystal display (LCD) for increasing the Depth of Focus (DOF) of the imaging system as a whole. The lenses are spatially multiplexed in a random scheme onto the LCD. The axial irradiance distribution produced by each lens overlaps with the next one producing an extended focal depth. In section 7, we will show experimental results.

5 Control of the amplitude and phase in a liquid crystal spatial light modulator

In twisted nematic LCDs the amplitude and phase modulations are highly coupled [95], especially magnified by the tendency to decrease the thickness to enable the efficient addressing of the larger number of pixels. The reverse-engineering model proposed in [96] is able to account for the electro-optical properties

of the twisted nematic LC-SLMs, allowing the accurate calculation of its complex amplitude transmission as a function of the applied voltage. In this model we take into account that the LC molecules in the vicinity of the faces of the LC-SLM (edge layers) have a constraint to reorient with the applied voltage V. Based on this model, together with a novel elliptically polarized light approach, we demonstrated an optimization procedure [97, 98] leading to amplitude-only and phase-only modulations for thin LCDs. This optimization was performed for a single wavelength, as in general the chromatic dispersion of the liquid crystal produces a large variation of the complex amplitude transmission as a function of the wavelength. When using non-monochromatic illumination it is also important to take into account the variation in the performance of the external polarization devices, mainly the retardance of the wave plates used to generate and detect elliptically polarized light. In [97] we studied and compared various calibration procedures to obtain the retardance of a wave plate.
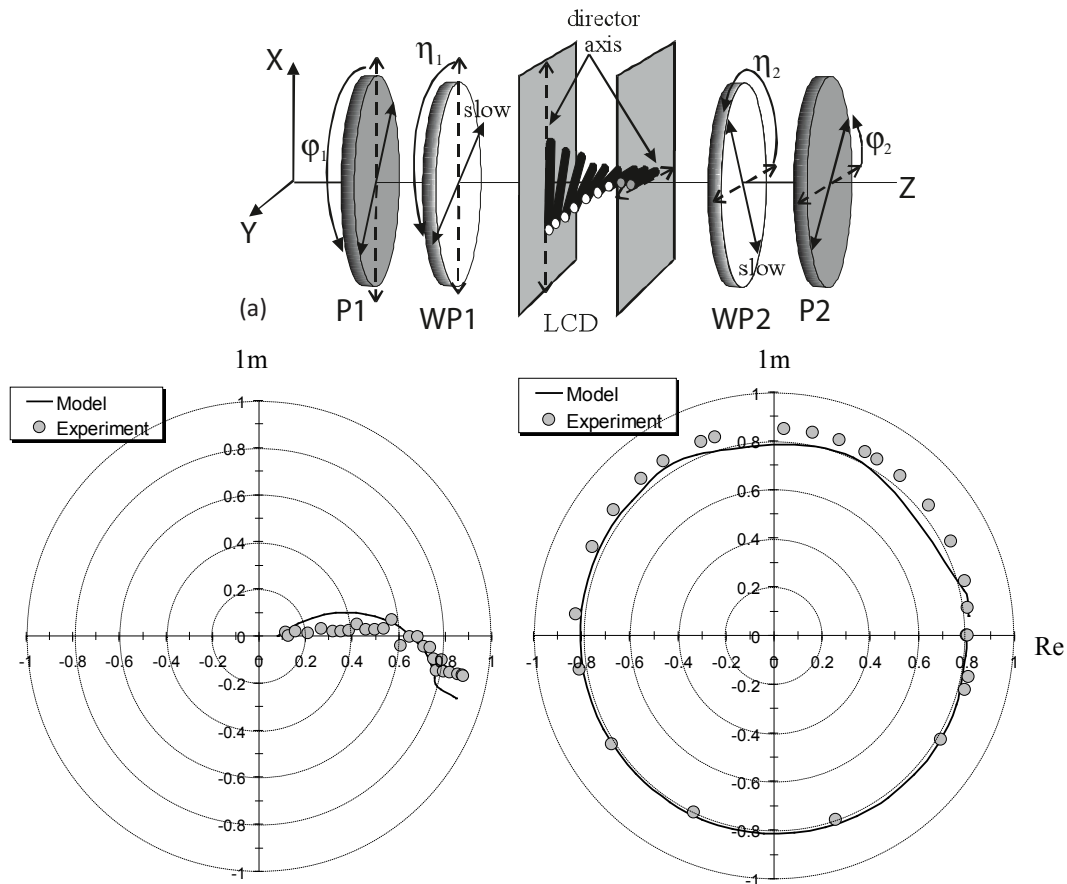

Fig 7. (a) Setup to generate and detect elliptically polarized light. P, polarizer; WP, wave plate. (b) and (c) are the optimum amplitude-only and phase-only modulations obtained for $\lambda = 458$ nm.

Our goal is to optimize the modulation of the LCSLM for the whole visible spectrum. In this work all experimental results which will be presented in the following sections are produced with a Sony liquid crystal panel, model LCX012BL, extracted from a Sony video projector model VPL-V500. We are interested in using the LC-SLM in the amplitude-mostly regime or in the phase-mostly regime. We consider the general case of elliptically polarized light, shown in Fig 7(a), where the LC-SLM is sandwiched between a pair of polarizers, P, and waveplates, WP. In Figs 7(b) and 7(c), we show respectively the optimum amplitude-only

and phase-only modulations obtained, illuminated with the 458 nm line of an Ar$^+$ laser. The retardance of the input and output wave plates at 458 nm is, respectively 125º and 94.5º. We observe the excellent agreement between the results simulated using our model and the experiment. Furthermore the modulations obtained are nearly equal to the ideal ones. In the amplitude-only configuration the angles for the transmission axis of the polarizers and for the slow axis of the wave plates are ($\varphi_1 = 116º$, $\eta_1 = 96º$; $\eta_2 = -7º$, $\varphi_2 = 62º$). In the phase-only configuration these angles are ($\varphi_1 = 26º$, $\eta_1 = 0º$; $\eta_2 = 11º$, $\varphi_2 = -16º$).

We extend the optimization procedure proposed in [97] to broadband spectrum in order to obtain the orientation of the polarizing devices for the optimum configuration for all the wavelengths. For the optimization procedure we must define a figure of merit which takes into account the characteristic properties desired for the amplitude-mostly regime or for the phase-mostly regime. To sample the visible spectrum we consider three wavelengths covering the red, green and blue regions of the spectrum: 633, 514 and 458 nm. These are standard wavelengths obtained from laser systems: 633 nm from a He-Ne laser, 514 and 458 nm from an Argon ion laser.

In the case of the amplitude-mostly regime we have that the amplitude should have a large dynamic range and should be as linear as possible, the minimum of intensity should be ideally zero to avoid background light, and the phase dynamic range should be zero. We have to attain all these properties not at one wavelength but along the whole visible range. In particular, they should be attained simultaneously for the three wavelengths selected to sample the whole visible spectrum. We consider the LCD inserted between two linear polarizers. The results obtained for the transmission axis of the input and output polarizers are respectively, $\varphi_1 = 90.3º$ and $\varphi_2 = 89.7º$, expressed in each case with respect to the director axis at the input face and at the output face of the LC-SLM.

In Fig 8, we show the theoretical amplitude and phase modulations predicted from our model together with the experimental measurements for the three wavelengths 458 nm, 514 nm and 633 nm. The X-axis represents the gray level, which is related with the voltage sent to the LC-SLM. We can see that there is a good agreement between theory and experiment for the three wavelengths. In the amplitude plot, Fig 8(a), we see that the minimum of amplitude is quite low for the three wavelengths (about 0.1): we note that this corresponds to such a very low value about 0.01 for the intensity transmission. The maximum value of amplitude transmission is attained at a different gray level for each of the three wavelengths. For the application in section 8.1 we need a single-valued calibration curve. This can be obtained by using the gray level range till 210 (indicated by the dashed line on the figure).
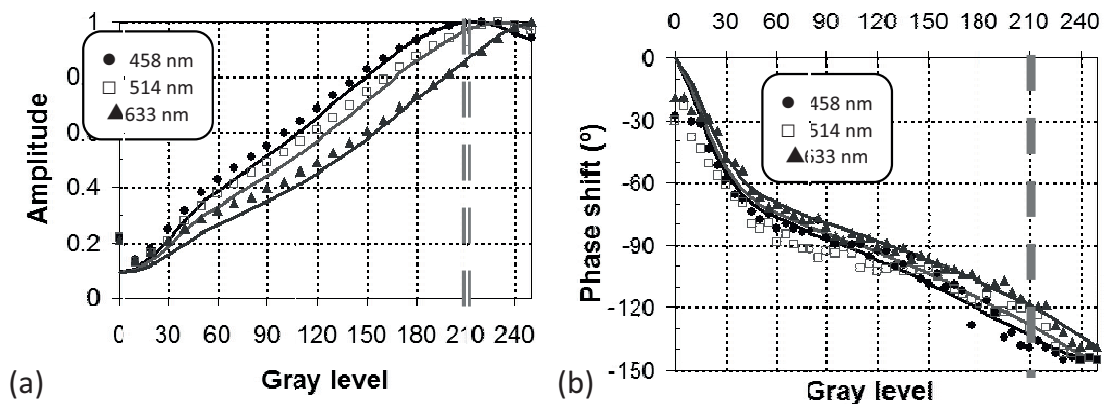

Fig 8. Complex amplitude modulation for the optimum amplitude-only regime for the three wavelengths 633 nm, 514 nm and 458 nm. Symbols correspond to the experimental measurements and continuous lines to the theoretical predictions. (a) Amplitude and (b) Phase modulations.

Looking at the phase graph, in Fig 8(b), we see that the phase dynamic range is about 140º along the gray level range from 0 to 210. Nevertheless, we see that the largest phase variation takes place in the gray level range 0-40 where the amplitudes values are low (the intensity transmission values are about 0.01 as noted earlier). So, the effective phase range can be considered much lower than 140º. In the gray level range 40-210 the phase variation is about 60º. We will see in the following section that this is not a limiting factor for the present application and we can consider this transmission as an amplitude-mostly regime.
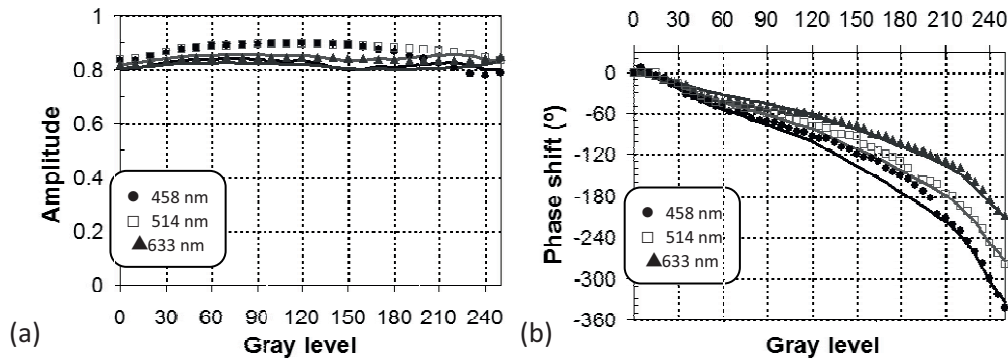

Fig 9. Complex amplitude modulation for the optimum phase-only regime for the three wavelengths 633 nm, 514 nm and 458 nm. Symbols correspond to the experimental measurements and continuous lines to the theoretical predictions. (a) Amplitude and (b) Phase modulation.

To obtain a phase-only regime for the LCD valid for a wide range of wavelengths we extend the optimization procedure proposed in [97]: now the figure of merit to be optimized takes into account several wavelengths simultaneously which cover the whole visible spectrum. The LCD is inserted between two sets composed by a polarizer and a wave plate. To obtain a phase-only regime using only polarizers is not possible since the LC layer in modern LCDs is not thick enough to provide the necessary phase dynamic range [97]. This can be increased by applying elliptically polarized light, thus adding two external wave plates at the entrance and exit faces of the LCD, as in the set-up in Fig 7(a). In this work we used zero order quarter wave plates (Meadowlark Optics) designed for the 458 nm. We measured the retardance values for the two wave plates: 89.4º at 458 nm, 76.2º at 514 nm and 58.3º at 633 nm. In Figs 9(a) and (b), we plot respectively the amplitude and the phase modulations versus the gray level for the three wavelengths (633, 514 and 458 nm). We show both the experimental values (symbols) and the predicted values (continuous lines) by our model [96]. There is a very good agreement between both values. We see that the transmission is very uniform and almost equal for the three wavelengths. The phase dynamic range is close to 360º at 458 nm, and it is still very high, 210º, at 633 nm. The results obtained for the transmission axis orientation of the input and output polarizers are, respectively 6º and 53º, and for the fast axis of the input and output wave plates, 78º and 19º, respectively. The angles are expressed with respect to the director axis at the input face of the LCD for the input elements, and with respect to the director axis at the output of the LCD for the output elements.

6 Amplitude filters encoded in amplitude or phase-mode in an LC-SLM

6.1 LC-SLM in the amplitude mode

As described in section 2, by changing the amplitude transmission it is possible to modify the PSF of the system both in a transversal plane (resolution, apodization), and along the axis (depth of focus, multifocus). In order to demonstrate, on one side, the programmable amplitude pupil filters written onto the LC-SLM in the amplitude-only or in the phase-only regimes, and on the other side, multiplexed onto the diffractive lens as the programmable amplitude apodized Fresnel lens (PAAFL), among the various

filters described in section 2, we concentrate on three specific non-uniform transmission filters: $P(r) = 1 - 4r^2 + 4r^4$, $P(r) = 1 - r^2$ and $P(r) = r^2$. Our motivation to choose these filters has been to be able to show a complete overview of the interesting possibilities that non-uniform transmission filters may offer in the design of optical systems. Both in section 6.1 and 6.2, the results we present are given using an alternative expression for the magnitude in Eq (1) since we are interested in making the usual expression for the defocus coefficient explicit. This expression is the following,

$$U(\rho, W_{20}) = 2\pi \int_0^1 P(r) \exp\left[i\, 2\pi\, W_{20}r^2\right] J_0\left(2\pi\, \rho\, r\right)r\, dr \tag{26}$$

where ρ is the radial coordinate in the image, W_{20} is the defocus coefficient, r is the radial normalized coordinate in the pupil plane, and $P(r)$ is the radial amplitude distribution in the pupil plane, that is, the filter function. To express the calculations with respect to the transverse, s, and to the axial, z, lab coordinates we have to scale the normalized PSF coordinates as follows,

$$s = \frac{\lambda}{NA}\rho, \quad z = \frac{2\lambda}{NA^2}W_{20}, \tag{27}$$

with NA the numerical aperture of the system.

In Fig 10(a), we show the theoretical axial responses produced by the different filters. For each filter, the intensity values are normalized by its maximum intensity value, that for all the filters occurs at the BIP. In *curve a* we display the results corresponding to the clear aperture. For this case, the intensity oscillates according to a sinc-squared function as the distance W_{20} to the BIP increases. The response for the axial hyperresolving filter corresponds to *curve b*, where we can see that the first axial minimum is closer to the BIP than the first axial minimum corresponding to the uniform transmission pupil, *curve a*. Then, the depth of focus decreases, while we can see that the secondary maxima are highly increased in value. So, we consider this type of filter as a multifocus filter. The filters $P(r) = 1 - r^2$ and $P(r) = r^2$ exhibit identical axial behavior. We mention that the maximum intensity values for both filters are also equal. The two filters correspond respectively to *curve c* and to *curve d*, which are actually overlapped. We can see that the two filters have an axially apodizing behavior with no secondary maxima along the axis.
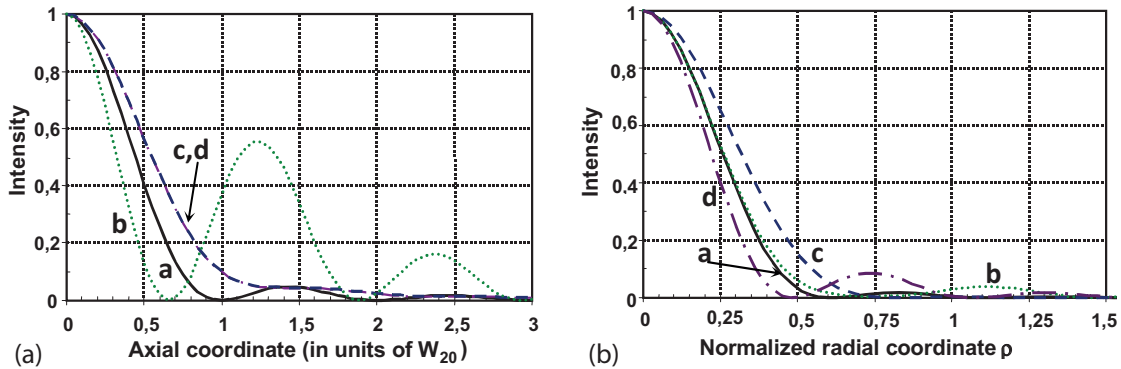

(a)

(b)

Fig 10. Numerically calculated intensity (a) along the axis and (b) in the BIP for the amplitude pupil filters: **a**, uniform transmission; **b**, axial hyperresolving fiter ($P(r) = 1 - 4r^2 + 4r^2$); **c**, transverse apodizing filter ($P(r) = 1 - r^2$); **d**, transverse hyperresolving filter ($P(r) = r^2$).

In Fig 10(b) we show the numerical results corresponding to the transverse behavior of the filters at the best image plane (BIP). As in Fig 10(a), for each filter the intensity values are normalized by its maximum intensity value. In comparison with *curve a*, corresponding to the clear aperture, we can see the apodizing effect of the filter $P(r) = 1 - r^2$, *curve c*, with the increased width of the central maximum. The hyperresolving effect of the filter $P(r) = r^2$, *curve d*, is also evident in comparison with *curve a*. The

remaining filter, the axial hyperresolving, *curve **b***, produces a slight increase in the width of the central maximum with respect to the clear aperture.

In [43] we demonstrated the feasibility of the programmable apodizers using a LC-SLM working in the amplitude-mostly regime. This regime was obtained by inserting the LC-SLM between two polarizers. The results obtained were in good qualitative agreement with the numerical predictions. However, the use of only polarizers does not permit to obtain an amplitude-only configuration. Then, in [45] we obtained the results with the LC-SLM in the amplitude-only configuration with elliptically polarized light shown in the previous section 5. This configuration provides a coupled phase-shift range as low as 18 degrees, thus, this can be considered an amplitude-only modulation, and a more quantitative analysis of numerical and experimental results can be performed, as we will review in the following. The scheme for the experimental set-up is presented in Fig 11. Light from an Ar^+ laser with a wavelength of 458 nm is expanded and an optical system is responsible for the convergence of the light beam. The LC-SLM is inserted between the two polarizers (P1 and P2) and the two wave plates (WP1 and WP2).
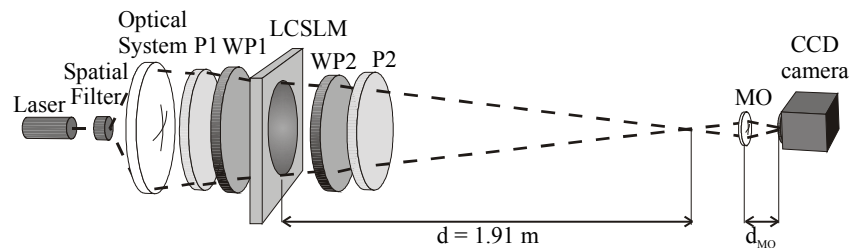

Fig 11. Scheme of the optical set-up for programmable apodizers.

The aperture of the filter on the LC-SLM has a diameter of 408 pixels (16.85 mm). The aperture of the filter is acting as the limiting aperture of the system and the exit pupil coincides with the position of the LC-SLM. The PSF is magnified using a microscope objective and imaged onto a CCD camera. In order to examine various defocus planes, the distance d_{MO} between the microscope objective *MO* and detector is fixed and the entire objective/detector system is translated.
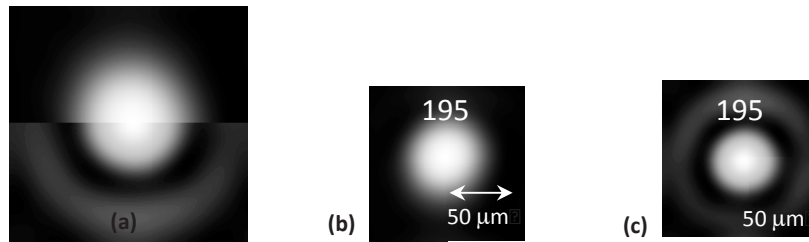

Fig 12. Experimental measurements at the BIP of the intensity of the focused spot. (a) Combination of saturated images (upper half, filter $P(r) = 1 - r^2$; lower half, filter $P(r) = r^2$). (b) Filter $P(r) = 1 - r^2$. (c) Filter $P(r) = r^2$.

First, we show results for the transverse apodizing ($P(r) = 1 - r^2$) and the transverse hyperresolving ($P(r) = r^2$) filters. Theoretically, as we have seen in Fig 10(a), the response along the optical axis is exactly equal for both filters. Experimental measurements are in accordance with this result. Actually, the interesting properties of these filters are at the BIP. In Fig 12 we show the BIP images captured for both filters. The images have been digitally saturated in order to show the sidelobes. In Fig 12(a) we have combined the focused spots for the filter $P(r) = 1 - r^2$ (upper half) and for the filter $P(r) = r^2$ (lower half). We can clearly see the larger width of the central maximum for the filter $P(r) = 1 - r^2$ with respect to the filter $P(r) = r^2$. We can also distinguish the radial sidelobe for the filter $P(r) = r^2$. On Fig 12(b) and on Fig 12(c), we display the intensity value (in gray level) measured at the peak for both filters. The peak intensity is exactly equal

in both images as numerically predicted. On the images we also show the equivalent transverse scale in micrometers. We use this scale to measure the position of the maxima and minima at the BIP.

Now, we show results with the multifoci filter ($P(r) = 1 - 4r^2 + 4r^4$). In Fig 13 we show the images captured for this filter at its characteristic axial positions. The images have been taken under identical conditions of illumination in order to compare the intensity values between them. We have digitally saturated the images in Fig 13 to show the sidelobes.
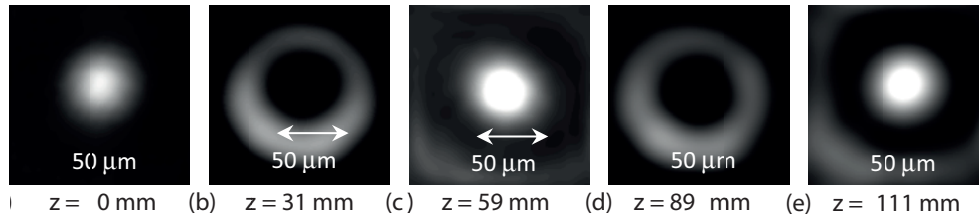

| z = 0 mm | (b) z = 31 mm | (c) z = 59 mm | (d) z = 89 mm | (e) z = 111 mm |

Fig 13. Experimental measurements of the response for the amplitude filter $P(r) = 1 - 4r^2 + 4r^4$ at the following planes. (a) BIP; (b) First axia minimum; (c) First axial secondary maximum; (d) Second axial minimum; (e) Second axial maximum.

In this section we have validated the correct implementation of programmable pupil filters on an amplitude-only LC-SLM. The technique is easy to implement and should allow experimental results for various transmissive filters to be obtained easily. The big potential of this technique is that the video rate refreshment of the LC-SLM allows the filters to be rapidly changed for modifying the PSF of an optical system.

6.2 LC-SLM in the phase mode

We demonstrated in [44] the feasibility of the PAAFL on a LC-SLM working in the phase-only regime. This is the suitable regime to display the lens, as it is a phase-encoded element. Next we use the configuration given in previous section 5, to obtain the phase-only regime with the LC-SLM. Thus, the PAAFLs are generated on a phase-only media, however, the PAAFLs are complex amplitude functions. To display complex amplitude information on the LC-SLM in the phase-only regime, in [44] we extended to a quadratic phase carrier the method proposed by Davis *et al* [53] with a linear phase carrier. Furthermore, when displaying the PAAFLs we have to take into account the inherent equivalent apodization effect due to the pixelated structure of the SLM [56]. In [56] we demonstrated a technique to measure and compensate for this effect.

To implement the PAAFLs we use the experimental set-up shown in Fig 14. The set-up is very similar to the one presented to display the programmable apodizers, Fig 11. Light from an Ar$^+$ laser with a wavelength of 458 nm is filtered, expanded, and collimated. Then it is sent through the LC-SLM that has been inserted into an architecture of polarizing devices composed of two wave plates (WP) and two polarizers (P). Note that in this set-up, when compared with Fig 11, the focusing function is performed by the PAAFL displayed on the LC-SLM. The Fresnel lens in the PAAFL has a focal length of 1 meter and a radius of 204 pixels (8.4252 mm). With the lens we have encoded the three different amplitude filters already commented: the transverse apodizing filter, the transverse hyperresolving filter, and the axial hyperresolving filter,
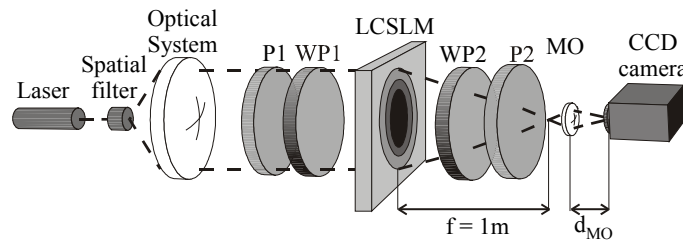

Fig 14. Scheme of the optical set-up for PAAFLs.

First, we demonstrate the distorted PSF that we obtain when we do not compensate for the inherent equivalent apodizing effect due to the finite extent of the pixel [56]. In Fig 15, we show the experimental images obtained with the filters $P(r) = 1 - r^2$ (Fig 15(a)) and $P(r) = r^2$ (Fig 15(b)), when we directly send the PAAFL to the LC-SLM and do not compensate for the inherent apodizing effect. We can see that due to the inherent equivalent apodizing effect the peak values for both filters are clearly different: 190 and 95 (in gray level). We know that both peaks should have identical value.
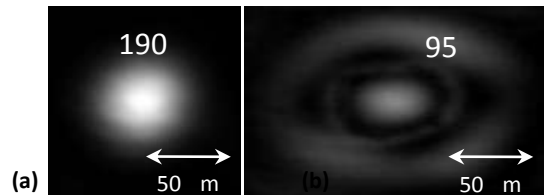

Fig 15. Experimental images of the intensity of the focused spot when the inherent apodizing effect is not compensated. (a) transverse apodizing filter; (b) transverse hyperresolving filter.

In Fig 16, we show the experimental images obtained when we compensate for the equivalent amplitude transmission in the plane of the pupil, measured by means of the technique proposed in [56]. Now we are compensating both the inherent equivalent apodizing effect due to the pixelation, and the residual aberrations in the system. We can see that we obtain nearly the same value for the peak intensity with the two filters. In Fig 16(b), we can clearly distinguish the secondary maximum (a ring). In Fig 16(b) the intensity in this ring has almost the same value as the central peak, while in Fig 16(b) were the inherent equivalent apodizing effect has been compensated both values are in accordance with theoretical results. We note that we use a LC-SLM that is almost free of aberrations.
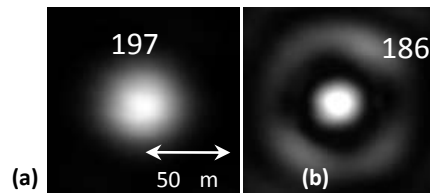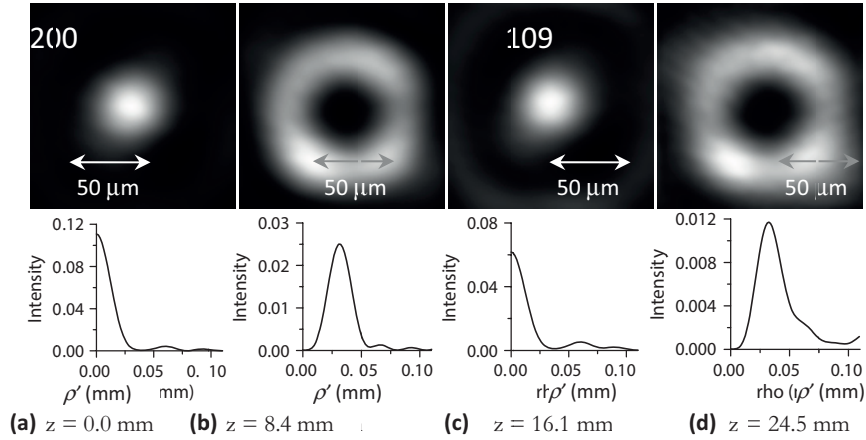

Fig 16. Experimental images of the intensity of the focused spot when the equivalent amplitude profile in the pupil has been compensated. (a) transverse apodizing filter; (b) transverse hyperresolving filter.

To demonstrate the capability of the method to generate PAAFLs we also show here the results obtained when generating the filter $P(r) = 1 - 4r^2 + 4r^4$ encoded onto the Fresnel lens. We have compensated for the inherent apodizing effect. In Fig 17, we show the experimental images captured at different defocused planes. They have been digitally saturated to show the sidelobes in the transverse response. The numerically calculated transverse responses at these planes are shown in the second row. The intensity values in the numerical graphs are normalized with respect to the numerically calculated peak value for the clear aperture. The *X*-axis in the numerical graphs is scaled to the radial lab coordinate ρ' in millimeters. The origin of coordinates (ρ' = 0 mm) corresponds to the center of the experimental images in the first row. The planes of Figs 17(a) and (c) show the principal maximum and the first secondary maximum, and the planes of Figs 17(b) and (d) show the first and the second axial minimum. These planes coincide with the axial positions predicted numerically, which is indicated in millimeters underneath each figure.

In Fig 17(b) and Fig 17(d), which correspond to the positions of the minima along the axis, the transverse responses present a ring. The positions for these rings, which can be determined by using the length scale on the figure, agree very well with the numerical prediction (second row). In Fig 17(a) and Fig 17(c), we show the values of the gray levels for the peak intensity for the best image plane (200) and for the first secondary maximum (109). The experimental ratio of the intensity of the first secondary maxima

with respect to the peak intensity in the best image plane is 0.55, which agrees very well with the theoretical ratio (0.56).


(a) z = 0.0 mm   **(b)** z = 8.4 mm   **(c)** z = 16.1 mm   **(d)** z = 24.5 mm

Fig 17. Experimental images of the intensity at various defocus planes for the axial hyperresolving filter compensated for the inherent equivalent apodizing effect. In the first row the experimental images are shown, in the second row the corresponding numerically calculated transverse responses are shown.

The agreement between the experiment and the numerical predictions has been excellent. Thus, we have demonstrated both qualitatively and quantitatively the feasibility of producing PAAFLs, which can modify both the PSF and the focal length in real time.

7 Increase the depth of focus using pupil filters or multiplexed lenses in an LC-SLM

7.1 Phase-only pupil filters

Next we show the experimental results obtained with some of the filters [46-47] described in Table 5 in section 4 of this paper. The phase only filter under discussion correspond to five equally area annuli. Specifically, we show the results with the filter f_1 and the filter psm. For the sake of comparison we also show the corresponding results for the clear aperture. We will use the filters to produce the image of an extended object.
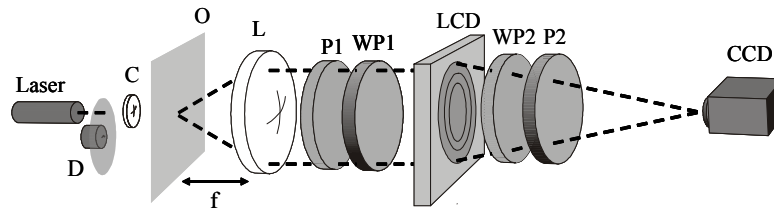
Fig 18. Scheme of the imaging set-up for extended objects. D is a rotating diffuser, C a condenser, O is the object placed in the focal plane of lens L. P1 and P2 are polarizers, WP1 and WP2 are wave plates that together with the liquid crystal display LCD conform the pure phase modulator used to display the diffractive lenses. An image of O is captured by a CCD camera.

In Fig 18, we show the experimental set-up used for imaging extended objects both in the present section 7.1 and in the next section 7.2. The filters have been implemented in the LC-SLM already described in section 5, working in phase only regime using the elliptically polarized light configuration. The illumination wavelength was λ = 458 nm (blue line of an Ar^+ laser) and the numerical aperture was given as NA = 0.01. A rotating ground glass D was used to disturb the coherence of the laser light source. So the case of complete incoherent illumination can be supposed. The object O is uniformly illuminated by means of the

condenser C. The phase-only filter is multiplexed onto a diffractive lens and addressed onto the LC-SLM. The object is placed in the focus plane of lens L, in this way it is imaged in the focal plane of the diffractive lens shown in the LC-SLM. The images of the extended object are captured by a CCD camera at the end of the system.

As an example of the capabilities of the SLM to produce this type of phase only filters, we show in Figs 19, 20, and 21 the results corresponding to the filters of Table 5 in section 4. A sector star, also named Siemens star, was used as an imaging object. A sector star is equivalent to gratings of variable periods. The number of sectors is equal n. First, the best image plane for the optical system without filter was located and it is called $z = 0$. From this plane the CCD camera was shifted between $z = \pm 3$ (in normalized units), in steps of 0.5 and an image was recorded in every plane. The real coordinates are given by $z_{real} = z\, 2\lambda/NA^2$

The image intensity, produced from the sector star, is depicted in Fig 19 for the imaging lens without any filter. The best image plane ($z = 0$) shows an image that has to be used for comparison. One can see the sector star with a good contrast in the outer part. The central part shows a small area where the star is not resolved.
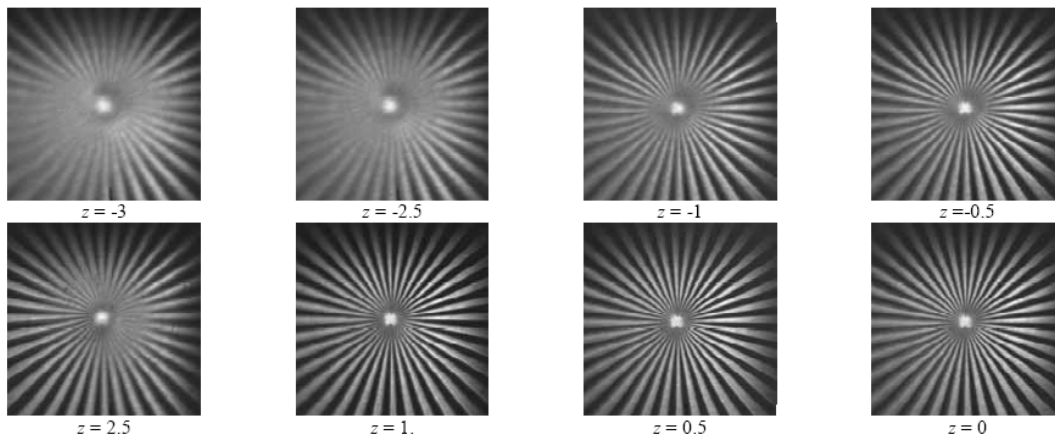

Fig 19. Image intensity caused by the sector star input in the optical system without any filter in different planes along the axis.

The rest of the images in Fig 19 show the expected results from the discussion in the previous section 4. We have images of high contrast and a given resolution in the range of $z = \pm 0.5$; for the rest of images $z > \pm 1$ shown in Fig 19, the area of the central part determined by the unresolved grating frequencies increases and the contrast all over the image is reduced.
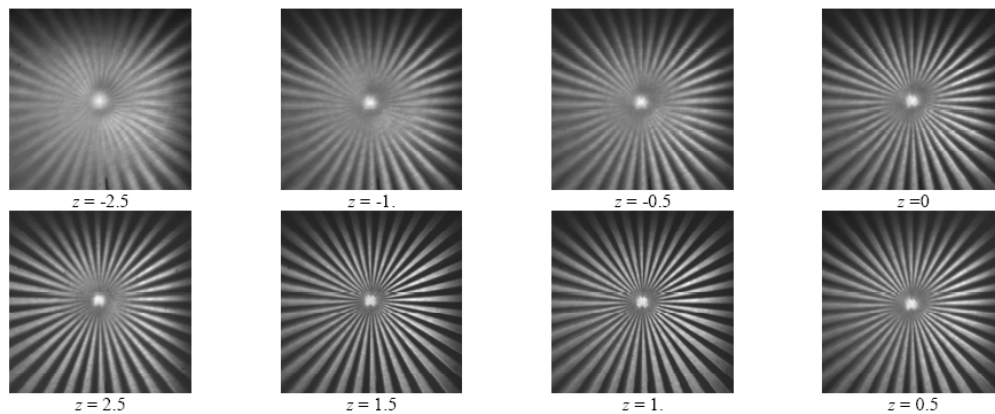

Fig 20. Images of the sector star object for filter f_2 in different planes along the axis.

Figure 20 shows the images produced by the sector star with filters f2. The filter f2 creates the best image at $z = 1$ in accordance with the results in section 4. The image quality (resolution and contrast of high spatial frequencies) is very similar to the image without filter. This means that the effect of the filters is the shift of thebest image plane. We see that the use of only five rings is enough to encode a convergent/divergent lens without apparent loss of quality.

Figure 21 gives the experimental results for psm filter. From the discussion of the merit functions in section 4 we expect, that the psm-filter gives two focal images along the optical axis at $z = \pm 2.5$. A loss of image contrast is obvious in Fig 21 for the psm-filter in the best image planes. The best image plane is shifted to $z = \pm 2.5$.
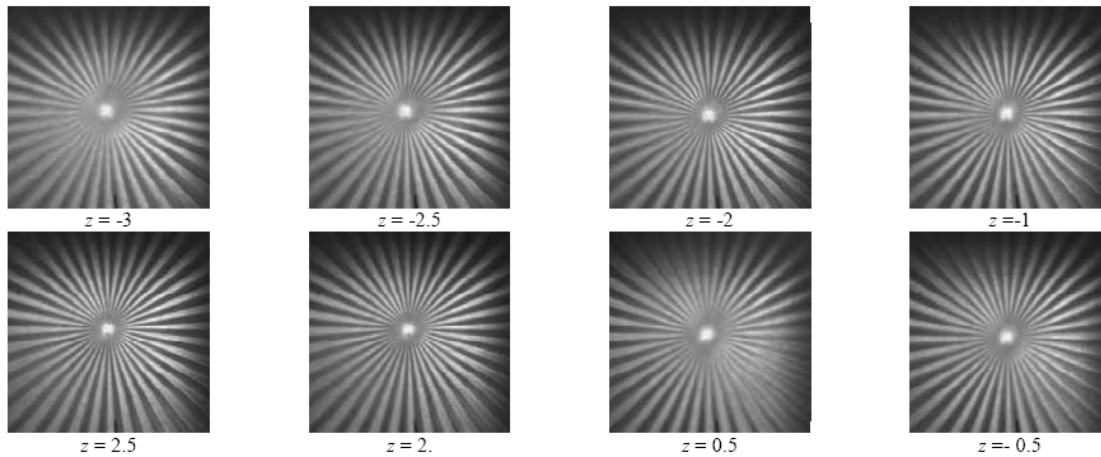

Fig 21. Images of the target object for psm-filter in different planes along the optical axis.

7.2 Multiplexed lenses

In this section we describe the method and we present some experimental results dealing with the increase of the DOF by spatially multiplexing diffractive lenses with different focal lengths, as given in [64]. Each lens is designed in such a way that lenses with consecutive focal lengths provide amplitude distributions along the axis that overlap. In a another paper [69] we have shown that among the different multiplexing possibilities, random multiplexing gives place to a system whose point spread function has reduced transversal sidelobes so, it is adequate to image extended objects. The multiplexed DOE is then implemented onto the LC-SLM in the phase-only configuration shown in Fig 7(c) in section 5. We note that the generated lenses have a 480 pixels diameter which is equivalent to 19.68 mm. The sampling of a Fresnel lens causes the appearance of multiple lenses when the sampling frequency is lower than the Nyquist frequency. To avoid this effect we design lenses with a focal length of about 100 cm for the blue line of an Ar laser ($\lambda = 458$ nm).

In the random multiplexing technique the aperture is divided in sub apertures of (P × P) pixels, each sub aperture will be randomly assigned to a different lens, and then the transmission of the pixels of this sub aperture is taken from the corresponding lens. The random assignment is performed as follows. For each sub aperture of the pupil a random number k in the range (0, N) is generated. Let the number k fall in the range $j - 1 < k \leq j$ with j an integer number. Then the phase values of the sub aperture pixels are taken from the lens j. The results we present in this section correspond to sub apertures of (1 × 1) pixel size. We build three multiplexed lenses that cover a focal range from 92 cm to 108 cm, the first one resultant of multiplexing 9 lenses, the interval between consecutive focal lengths being 2 cm; a lens resultant of multiplexing 17 lenses, with 1 cm between consecutive focal lengths; and a lens resultant of multiplexing 33 lenses with a spacing of 0.5 cm between consecutive focal lengths. The focal depth range has been

chosen arbitrarily. We will show that we can implement a multiplexed lens with a number of lenses enough to produce a smooth (almost constant) axial response.

In principle the multiplexed lenses must produce focalizations at different planes since each of the constitutive lenses will focus in a different location. In order to study the effect of the random pupil and the defocused light on the final image, next we analyze the transfer function of the various diffractive elements. In order to compare the image quality of the single lens (SL) with the M9 and M33 multiplexed lenses, we have numerically calculated the Modulation Transfer Function (MTF) in the three cases. We have calculated the MTF in three planes, in the Best Image Plane (BIP, Z = 0 cm) and in two arbitrary chosen defocused planes: Z = –6 cm and Z = –10 cm, (6 cm and 10 cm closer to the LCD, respectively). To serve as a reference, Fig 22(a) shows the MTF produced by the a single lens (SL) of focal length 100 cm. We can see a very good response in the Z = 0 cm plane that is deteriorated strongly in the defocused planes. Figure 22(b) shows a zoom of a region of interest in Fig 22(a). We can see that in these range of spatial frequency there are a lot of contrast inversions. Each time that the MTF value is equal to 0, then a contrast inversion is produced. The image information that corresponds to those frequencies is lost, even if a post-processing is done. So, we expect a bad image quality in these defocused planes.
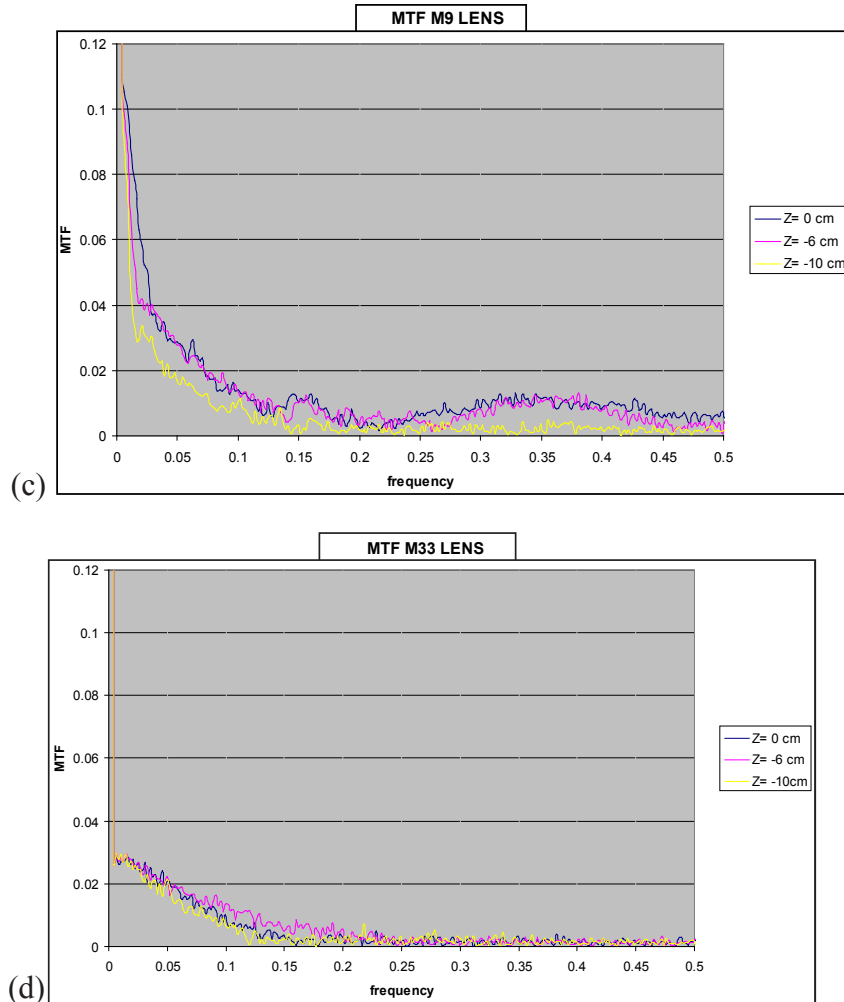

(a)

(b)
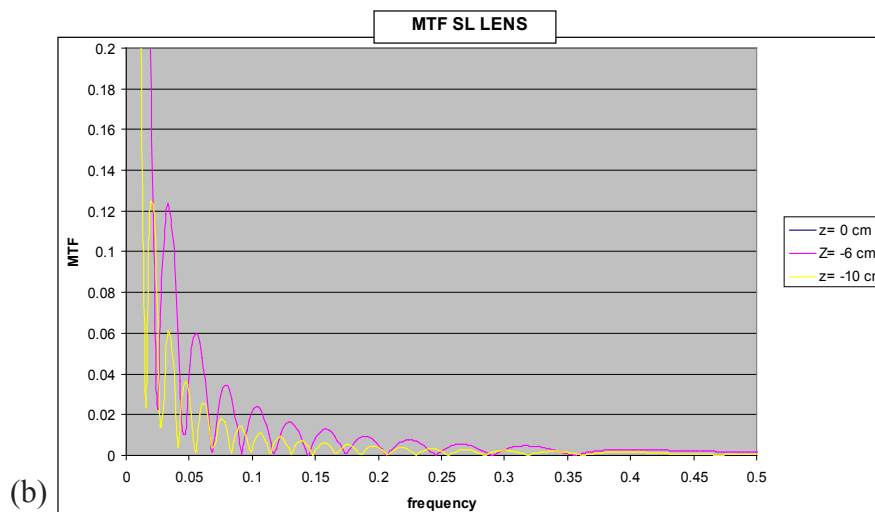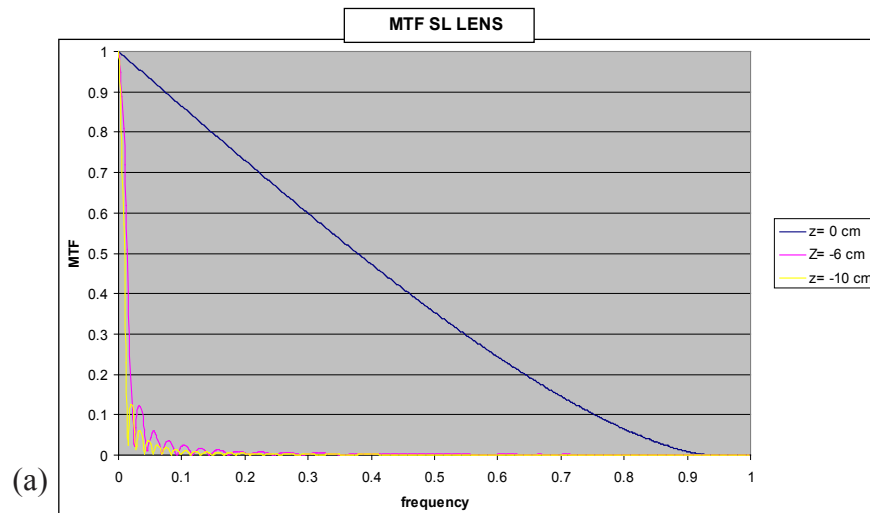
Fig 22. MTF plots: (a) Single lens in three planes; (b) single lens in three planes (zoom of the region of interest); (c) Nine multiplexed lens in three planes; (d) 33 multiplexed lens in three planes.

Figures 22(c) and (d) show the MTF produced by the M9 and M33 lenses, respectively in the BIP (Z = 0) and in two defocused planes. We note that for this random multiplexed lenses only one realization (the one used in the experiments) is evaluated and for this reason, there are random fluctuations in the MTF. If we compare Fig 22(c) and (d) with Fig 22(b) we see that the MTF in the BIP is obviously better for the SL. Both M9 and M33 lenses produce a strong descend in the MTF except for frequency 0. We expect a high background noise superposed to the object image. That can be appreciated in the experimental results that will be shown later. This background noise can be easily removed by subtracting a constant value to the whole image. This is the main drawback of the multiplexed lens, and a high dynamic range camera should be needed to capture correctly the image. But an advantage is that both the M9 and M33 lenses produce a far better response in the defocused planes. The M9 (Fig 22(c)) lens does not produce contrast inversions in the [0 - 0.1] frequency region (the SL lens produces at least 4 contrast inversion in that region, see Fig 22(b)). Nevertheless, one contrast inversion is appreciated in the [0.1 - 0.2] frequency region and another in the [0.2-0.45] frequency regions for Z = 0 cm and Z = –6 cm. The MTF of the M33 lens in the defocused planes is even better and there is a smooth decay with no trace of contrast inversions in the whole [0-0.5]

frequency region. So, we expect an image improvement in the defocused planes, especially with the M33 lens with respect to the SL lens..

In [64] we analysed both the PSF and the imaging properties of the multiplexed lenses for extended objects. In the present work we concentrate on the results dealing with the imaging of extended objects. We use the experimental set-up already described at the beginning of section 7.1. In order to compare experimentally the responses of the different multiplexed diffractive elements we displayed the lenses onto the LC-SLM and by shifting the CCD camera along the axis we registered the images of the extended object O at different planes in different experiments.

We use in this experiment two types of objects: a sector star (Siemens star) and a resolution target. In order to compare the responses of lenses with a different amount of multiplexed lenses we captured images of the Siemens star and the resolution target at Z = 0 with the M9 and the M33 lenses. The results are summarized in Fig 23.
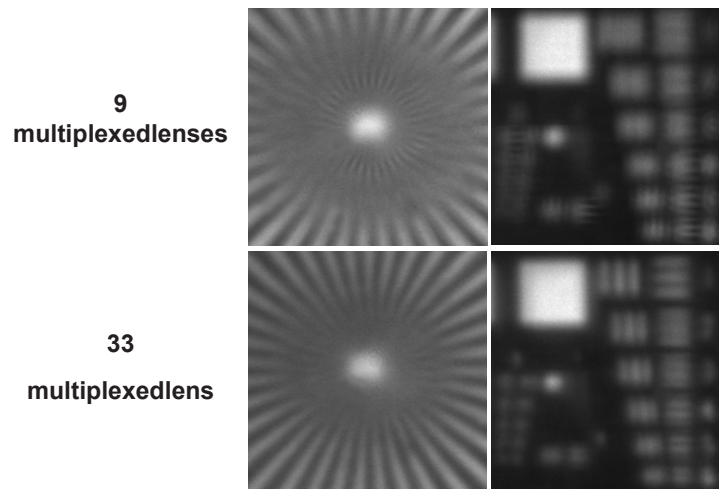

Fig 23. Images of an enlarged portion of the Siemens star and the resolution test captured at Z = 0 plane when 9 multiplexed lenses and 33 multiplexed lenses are used
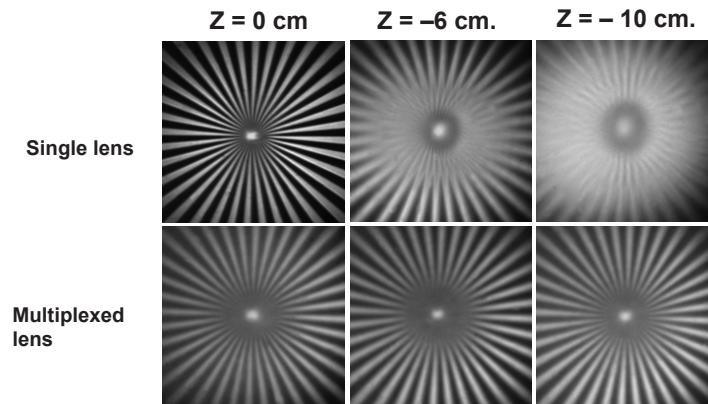

Fig 24. Images of the Siemens star captured at the best image plane (Z = 0) and defocused planes (Z = –6 cm and Z = –10 cm) when a single lens and a multiplexed lens (M33) are used.

It is noticeable from Fig 23 that some contrast inversions are evident for the M9 lens and zero values for the MTF appear in this case. We can also observe that the M33 lens does not produce contrast

inversions in those frequency regions. So, we conclude that the M33 produces a better response in the BIP. These results are in agreement with the MTF's shown in Figs 22(c) and (d).

Images of the Siemens star are shown in Fig 24. They are obtained by using the single lens and the multiplexed 33 lenses. The best image plane (BIP) for the single lens is placed at 100 cm from the LCD, we will identify this plane with Z = 0. We also show how the defocus degrades the image as the CCD is farther from that plane. Images were captured when the defocus is of –6 cm and –10 cm. When the multiplexed lens is used the images maintain their quality in the entire range of distances.

8 Polychromatic control using pupil filters in an LC-SLM

8.1 Supergaussian amplitude pupil filters to compensate chromatic axial variations

When interested in the general case of polychromatic illumination as it is the case in sections 8.1 and 8.2, an appropriate expression for the 3-D Point Spread Function (PSF) of an optical system is given by

$$G(\rho, W_{20}) = (1/\lambda^2) \left| U_\lambda(\rho, W_{20}) \right|^2 \tag{28}$$

where λ is the wavelength of the incident beam, $U(\rho, W_{20})$, shown in Eq (26), is the monochromatic amplitude on the image plane, where the defocus coefficient W_{20} controls de location of the corresponding plane.

In [48] we showed the application of non-uniform transmission apodizers written onto the LC-LSM to compensate for the longitudinal secondary axial color (LSAC) of a commercial optical system. In this application the LC-SLM is working in the amplitude-mostly regime obtained in section 5 for polychromatic illumination. The scheme of the experimental set-up is shown in Fig 25. Two laser beams (Ar$^+$ laser and He-Ne laser), providing the wavelengths used to sample the visible spectrum (red: 633 nm; green: 514 nm; blue: 458 nm) are aligned to pass through the spatial filter, whose pinhole acts as a point source for the optical system. Behind the optical system, a spatial light modulator system composed by the LC-SLM inserted between two polarizers is placed. The optical system forms the image of the pinhole at about 50 cm from the LC-SLM. The LC-SLM determines the limiting aperture, so it is acting as the exit pupil. To study the PSF given by the optical system we capture it with a CCD camera coupled to a microscope objective to magnify it. The system is illuminated successively with the three wavelengths and the three monochromatic PSFs are captured with a black and white CCD camera. To consider an equienergetic illuminant, before each measurement, we control with a radiometer that the intensity incident on the system from each of the wavelengths is equal. The optical system in this set-up is a Zoom Nikon ED, AF Nikkor 80-200 mm, with *f number* ranging from 2.8 - 22.
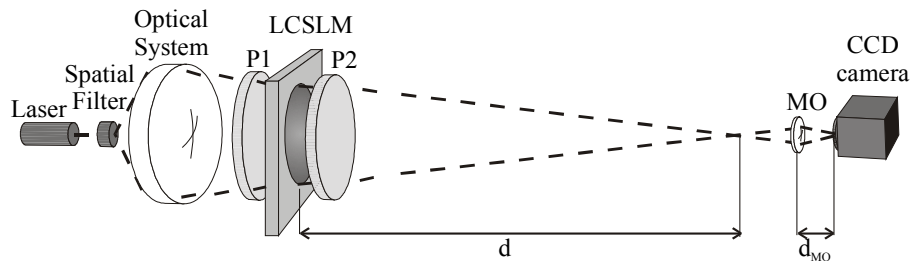

Fig 25. Scheme of the imaging set-up with the optical system under analysis. The aperture of the LC-SLM (16.52 mm of diameter) determines the exit pupil of the system. P1 and P2 are the polarizers; MO is the microscope objective. The distance d from the exit pupil to the image plane is about 50 cm; the distance d_{MO} is fixed to capture magnified images with the same magnification.

The first result that we obtained with the set-up in Fig 25 is that the BIP, defined as the plane where the value of the axial intensity is a maximum, varies with the wavelength as follows: 466.21 mm for the blue, 465 mm for the green and 468.16 mm for the red. The distance is measured with respect to

the exit pupil of the system (LC-SLM position). This variation for the BIP location is due to the LSAC for the refractive optical system. To compensate the effect of the LSAC, we proposed the use of an axial apodizing filter, i.e. a filter increasing the depth of focus (DOF). The family of the supergaussian filters, described in section 3, is well suited for this task [23]. The shape of these filters can be varied by changing the value of the various parameters as presented in Eq (21). We have selected this family of filters because the parameters t_0, Ω and α have a direct influence in different quality criteria [23]. By changing t_0, *the width of each monochromatic PSF in a transversal plane is modified. When $t_0 < 0.5$ the width is increased while for $t_0 > 0.5$ is decreased. The parameter Ω directly influences the DOF. When Ω decreases, the DOF increases and the total transmitted energy decreases. When $\alpha = 1$, the axial distribution does not present secondary maxima: they appear for higher values of α, as the supergaussian filter becomes more similar to the annular filter.*

We use the LC-SLM in the amplitude-mostly regime (Fig 8 in section 5) to display a series of supergaussian filters to control the PSF for the optical system with polychromatic light. By shifting the CCD camera along the axis we register the PSF at different axial planes. We take the origin of the reference system at the BIP for the green. The experimental images that we show correspond to the BIP for the green ($z = 0$ mm) and the BIP for the red ($z = 3.16$ mm). These are pseudocolored images, composed using the three experimental monochromatic PSFs from the red, green and blue wavelengths as the RGB components for the pseudocolored image.
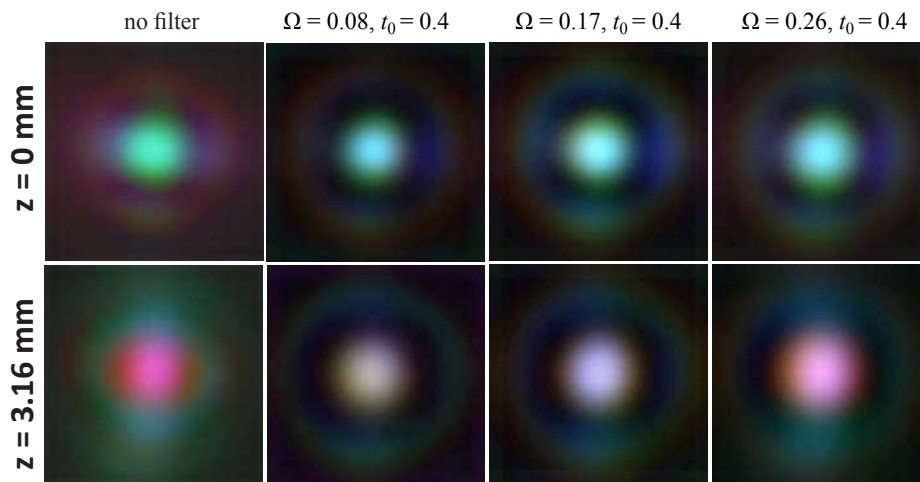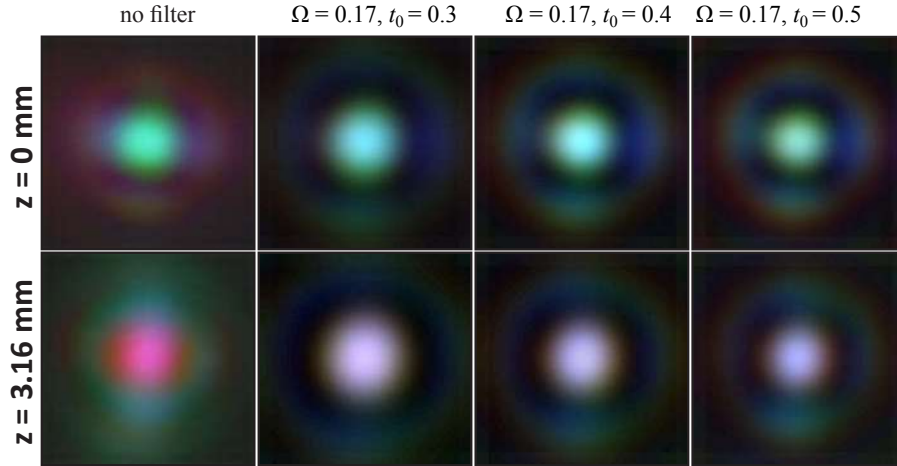

Fig 26. Pseudocolored images of the PSF obtained in the BIP for the green, $z = 0$ mm (first row), and for the red, $z = 3.16$ mm (second row), for the system without filter (column 1), and with supergaussian filters (columns 2, 3 and 4) centered at $t_0 = 0.4$ and for different widths given by Ω. In all cases the degree of the supergaussian is $\alpha = 1$.

In Fig 26 we show the pseudocolored images obtained for a series of supergaussian filters with a different width, i.e. Ω varies, in the BIP for the green (first row) and in the BIP for the red (second row). The parameters α and t_0 have equal values: $\alpha = 1$ and $t_0 = 0.4$. In this way, the width of the central maximum remains constant in the transverse response, but the DOF varies, decreasing as Ω increases. In the first column, we show the image obtained with the system without filter. We clearly observe the unbalance of energy between the three wavelengths due to the LSAC of the optical system, obtaining a mostly green image at the BIP for the green, and a mostly red image at the BIP for the red. The next three columns show the PSF obtained with the supergaussian filters with an increasing value for Ω. We see that the filters with lower Ω values ($\Omega = 0.17$, $\Omega = 0.08$) are able to equalize the intensity for the different wavelengths and they produce a chromaticity nearer to the white zone, corresponding to the equienergetic illuminant. The

higher DOF of focus for these filters is the responsible for this more homogeneous distribution of intensity at the two axial planes. Thus, we can apply a supergaussian filter with a low value of Ω to compensate the effects of the LSAC of the optical system. It is not interesting to choose a very low value of Ω since this would also reduce the amount of energy transmitted by the filter. A reasonable trade-off would be $\Omega = 0.17$.

Fig 27. Pseudocolored images of the PSF obtained in the BIP for the green, $z = 0$ mm (first row), and for the red, z = 3.16 mm (second row), for the system without filter (column 1), and with supergaussian filters (columns 2, 3 and 4) of the same width $\Omega = 0.17$ and centered in different positions given by t_0. In all cases the degree of the supergaussian is $\alpha = 1$.

In Fig 27 we show the pseudocolored images obtained for a series of supergaussian filters with a different position of the maximum, i.e. t_0 varies, in the BIP for the green (first row) and in the BIP for the red (second row). The parameters α and Ω have equal values: $\alpha = 1$ and $\Omega = 0.17$. With these filters the DOF should be similar, thus the pseudocolored image should have equal chromaticity at the maximum. What we control, in some range, is the resolution in the transverse plane, the PSF are more apodized for lower values of t_0. We show in the first column the experimental images for the system without filter (no filter) to serve as a reference. We see that the chromaticity of the images obtained with the three filters does not vary appreciably. On the contrary, the width of the PSF decreases as the value for t_0 increases.

With the experiments shown in Figs 26 and 27, we demonstrate that we are able to compensate the chromatic variations along the axis by increasing the depth of focus, and we are also able to modify the resolution in the transverse plane by varying t_0. The introduction of the filters using the LC-SLM allows for a dynamic control of the PSF depending on the criteria considered for the filter. Numerical results are provided in [48], which agree with the experiments.

8.2 Achromatization by spatially multiplexing diffractive lenses

In [69] we demonstrated the generation of diffractive singlets with equal focal length, i.e. achromatic, for various wavelengths simultaneously. To this goal we used the LC-SLM in the phase-mostly regime with polychromatic illumination, shown in Fig 9 in section 5, with elliptically polarized light. In particular, we consider the wavelengths 633, 514 and 458 nm, which can be thought as discrete RGB channels whose control allows to change the chromaticity in some optical system.

In Fig 28 we show the experimental set-up. With respect to the set-up shown in Fig 26, now the beam incident onto the LC-SLM is collimated, and the diffractive lens displayed onto the LC-SLM is the

only responsible for the focusing of the beam. We use two laser beams (Ar$^+$ laser and He-Ne laser) aligned to pass through the spatial filter. The LC-SLM determines the limiting aperture, acting as the exit pupil, with a diameter of 480 pixels (19.68 mm). We have generated lenses with a focal length of 1 meter. To evaluate experimentally the performance of the lenses we adjust the intensity incident onto the LC-SLM in such a way that it is equal for the three wavelengths. The point-spread function (PSF) is captured with a monochromatic CCD coupled to a microscope objective to magnify the image as in previous PSF-measuring set-ups.
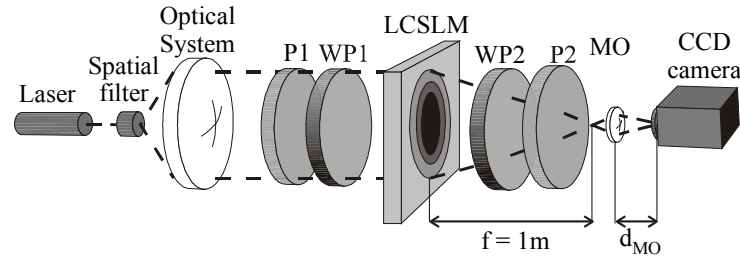

Fig 28. Scheme of the set-up for the achromatic diffractive singlet. The aperture of the LCSLM (19.68 mm of diameter) determines the exit pupil of the system. P1 and P2 are the polarizers; WP1 and WP2 are the wave plates; MO is the microscope objective.

The a diffractive lens varies strongly with the wavelength of the illumination. If a diffractive lens designed for a wavelength λ is illuminated with a different wavelength λ_1, the focal length shifts to $f'_1 = (f' \lambda)/ \lambda_1$. Furthermore, if we analyse the diffraction efficiency η of the lens for the primary focus we obtain, $\eta = \text{sinc}^2(1 - \Delta\varphi/2\pi)$, where sinc $(x) = \sin(\pi x)/\pi x$ and $\Delta\varphi$ is the maximum phase depth in each ring. In general, the maximum phase depth $\Delta\varphi$ varies with the incident wavelength, thus changing the diffraction efficiency. To overcome the wavelength dependencies of the focal length and the diffraction efficiency we proposed [69] to use spatial multiplexing strategies to generate the diffractive lens.

In Fig 29 we show the gray level plots for a variety of diffractive lenses designed with the same focal length. The Fig 29(a), (b) and (c) correspond to diffractive lenses designed for monochromatic illumination at 633, 514 and 458 nm, respectively, which hereafter we will refer as the red (R), the green (G) and the blue (B) channels. We see that the radii of the circular rings are different in the three cases. Any of these three lenses shows a dramatic chromatic focal dependence. We use two spatial multiplexing techniques to obtain the achromatization. In the first one, annular-sector multiplexing, the aperture is divided in N rings and kN sectors, with k a positive integer and N the number of channels to be multiplexed (3 in our case). In the first ring the channels are distributed in an ordered sequence, e.g. RGBRGB..., where the pixels of the first sector are taken from the lens corresponding to the Red channel, the pixels of the second sector from the Green channel, and so on. In the second and the third rings, the channels are shifted (GBRGBR....), (BRGBRG...) to make the distribution of the channels more uniform. In Fig 30(d) an example with 3 rings and 30 sectors is shown. In the second multiplexing technique, random multiplexing, the aperture is divided in subapertures which are randomly distributed among the 3 channels. We can change the weight of each channel by varying the probabilities (pr, pg, pb) with pr + pg + pb = 1. In Figs 29(e) and (f) two examples of the random multiplexing are shown in which the subapertures have a size of 8×8 and 1×1 pixels, respectively. In these figures the three probabilities are the same (pr = pg = pb). In the experiments several probability combinations have been considered as shown next in Fig 30.

We note that in principle the multiplexed lenses must produce various monochromatic focalizations: each of the three subapertures will focus in a different location each of the three wavelengths used in this work, thus, producing 9 monochromatic focalizations. Due to the equal focal length programmed in the three multiplexed lenses we have that three of these monochromatic focalizations are much more efficient

and coincide in the same plane, which is the focus plane of interest for us. The remaining 6 monochromatic focalizations have a lower efficiency and are defocused, therefore in the focus plane of interest they contribute as a noise background, which as we show in Fig 30 does not degrade the experimental results obtained.
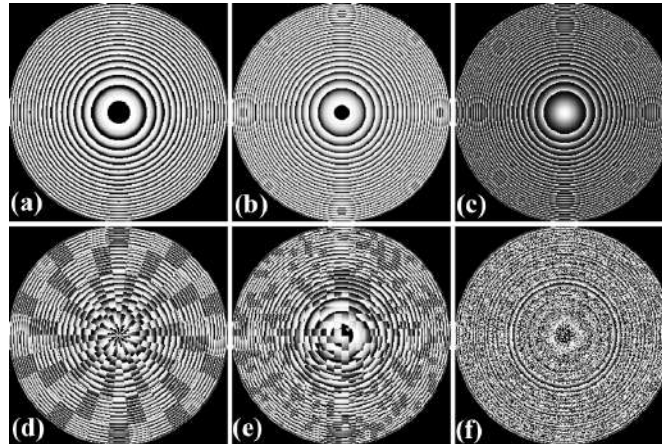
Fig 29. Gray level representation of diffractive lenses with equal focal length. In (a), (b) and (c) they have been designed for the wavelengths 633, 514 and 458 nm, respectively. In (d), (e) and (f) the lenses are the result of the spatial multiplexing with equal weights of the lenses (a), (b) and (c), with (d) divided in 30 sectors and 3 rings, (e) random multiplexing in areas of 8×8 pixels, and (f) random multiplexing in areas of (1×1) pixel.
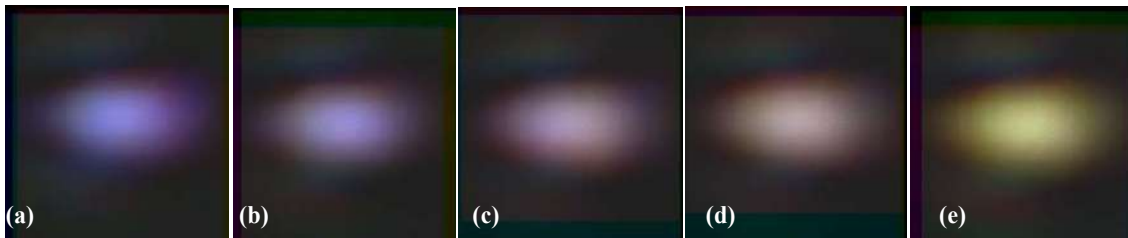
Fig 30. Pseudocolored PSF experimentally obtained using the random multiplexed lenses with (1×1) pixel areas, with RGB weights: (a) (1,1,2), (b) (1,1,1.7), (c) (1,1,1.5), (d) (1,1,1.3), and (e) (1,1,1).

We have both performed numerical calculations and experiments to measure the PSF using the annular-sector and the random multiplexing methods. We obtained better results using the random multiplexed lenses. The annular-sector multiplexed lenses produce a PSF with higher sidelobes and with a larger variation of the chromaticity along the PSF. In Fig 30 we show the experimental PSFs obtained using a random multiplexed lens divided in (1×1) pixel areas. The 3 monochromatic PSFs for RGB illumination have been pseudocolored to compose a single color image. The RGB weights assigned to the multiplexed lenses vary for the five PSFs and they are (1,1,2), (1,1,1.7), (1,1,1.5), (1,1,1.3) and (1,1,1), respectively for figures (a), (b), (c), (d) and (e). The asymmetry in the PSFs is due to an astigmatic phenomenon in the LCD reported in [103]. With these figures we want to show that by changing the weights for the various channels we can finely tune the chromaticity of the PSF. To this goal we have measured the value for the maximum gray level on each of the three RGB components. We have obtained respectively for figures (a), (b), (c), (d) and (e) that these maximum gray level values are (141,140,223), (159,150,217), (178,164,189), (190,179,173) and (209, 216, 148), where the three ordered elements in the arrays correspond, respectively to the value for each of the RGB component images. We see that as we go from Fig (a) to (e) the maximum gray level value for the B component decreases from 223 to 148. Simultaneously, the maximum gray level values for

the R and G components increase. This is consistent with the fact that the weight for the blue subaperture in the multiplexed lens is also decreased, whereas the area occupied by the red and green subapertures increase. We can also say that in each of the four PSFs the values for the maximum gray level for the R and G components are quite similar, which is consistent with the equal weights assigned to the R and G channels in the multiplexed lenses.

9 Summary

In the first part of this paper we have revised different techniques to design and analyze the influence of pupil filters on the behavior of an optical system. In section 2, we have described two methods for analyzing the response of an optical system with pupil filters. The first one is the calculation of Point Spread Function (PSF) both in the best image plane and along the axis. The PSF, and also the Modulation Transfer Function (MTF) (also used in some sections of this paper) are very well established as optical image criteria. Different parameters related with the quality of the image can be extracted from the PSF and from the intensity distribution along the axis. For instance, the radius of the first minimum on the transverse PSF gives information from the superresolution produced by a filter. In an analogue way, the Full Width at Half Maximum (FWHM) is a parameter obtained from the intensity distribution along the axis in order to study the Depth of Focus (DOF). For that reason, we also describe how to calculate some performance parameters that are easier to compute and are good for comparisons. The Transverse (G_T) and axial (G_A) gains, for instance, are excellent tools to analyze the transverse resolution and DOF produced by pupil filters. We also discuss in section 2 different ways of calculating these parameters for real and complex pupil filters.

In section 3, we study the transverse and axial behavior with amplitude transmission only filters. We describe some pupil filters that produce recognizable effects on the transverse (superresolution or apodization) or the axial (variation of the DOF) responses. We have discussed the pros and cons of using continuous varying filters versus binary (annular for instance) pupils. We also show results for supergaussian rings that are capable of tailoring the 3-D response of an optical system as a function of three parameters. We study some symmetry properties that can lead to specific behaviors and that are a good tool for pupil design. Some examples are shown with the supergaussian rings.

It is clear that the main drawback of using transmission only filters is the loss of light. For that reason, we study in section 4 the broader possibilities that complex amplitude filters offer. Two and three-zone ring pupils are analyzed firstly. Since the behavior can be very different, several designs are summarized remarking their possible applications. Secondly, five rings phase filters show their capability for moving the focal spot and more complex features. We also study in deep a very capable strategy to produce high focal depth. We show that multiplexing Fresnel lenses and, in some cases, combinations of them with some type of ring complex filters, high focal depths can be achieved.

We have shown, in section 5, how LC-SLMs can be optimized to provide the required amplitude and phase modulation, and for monochromatic or polychromatic illumination. The usual modulation regimes in most applications are amplitude-only and phase-only modes. Both have been obtained with a LC-SLM based on a twisted nematic LCD. To this goal an elliptically polarized light set-up is necessary. These modulation regimes enable to use the LC-SLM to display a wide variety of the pupil filters discussed in section 2-4. In section 6, we have reviewed results obtained for the implementation of amplitude pupil filters on the LC-SLM, where we have shown how they can be implemented both with the device in the amplitude-only and in the phase-only modes. In the latter case it is combined with a diffractive lens, the so-called PAAFL. We have shown, in section 7, a selection of experimental results dealing with phase-only pupil filters, where images of a sector star object are presented, recorded by implementing different annular phase pupil filters on a LC-SLM. We have further analysed how the combination of several diffractive lenses spatially multiplexed in a random scheme onto a LC-SLM enable to increase the DOF of an optical system. In section

8 (on one side), we have shown the application of non-uniform transmission apodizers written onto the LC-LSM to compensate for the longitudinal secondary axial color (LSAC) of a commercial optical system. In this application the LC-SLM is working in the amplitude-mostly regime for polychromatic illumination. On the other side, we have demonstrated the generation of diffractive singlets with equal focal length, i.e. achromatic, for various wavelengths simultaneously. To this goal the LC-SLM is used in the phase-mostly regime with polychromatic illumination.

Acknowledgments

References

1. Chung C S, Hopkins H H, *J Mod Opt*, 35(1988)1485.
2. Escalera J C, Yzuel M J, Campos J, *J Mod Opt*, 38(1991)1703.
3. Ojeda-Castañeda J, Andrés P, Díaz A, *Opt Lett,* 11(1986)487.
4. Cox I J, Sheppard C J R, Wilson T, *J Opt Soc Am A*, 7(1982)1287.
5. Escalera J C, Yzuel M J, Campos J, *Appl Opt*, 34(1995)1655.
6. Hegedus Z S, Sarafis V, *J Opt Soc Am A,* 3(1986)1892.
7. Sheppard C J R, Choudhury A, *Appl Opt*, 43(2004)4322.
8. Fukuda H, Yamanaka H R, *Jpn J Appl Phys*, 31(1992)4126.
9. Campos J, Escalera J C, Hild R, Muschall R, Nitzsche G, Yzuel M J, *Microelectron Engg,* 30(1996)103.
10. Sheppard C J R, Hegedus Z S, *J Opt Soc Am A*, 5(1988)643.
11. Yzuel M J, Escalera J C, Campos J, *Appl Opt*, 29(1990)1631.
12. Ojeda Castañeda J, Tepichin E, Díaz A, *Appl Opt*, 28(1989)2666.
13. Hild R, Yzuel M J, Escalera J C, *Microelectron Engg,* 34(1997)195.
14. Gu M, Sheppard C J R, *J Mod Opt,* 38(1991)2247.
15. Sheppard C J R, Gu M, *Opt Commun,* 84(1991)7.
16. Martínez-Corral M, Andrés P, Ojeda-Castañeda J, Saavedra G, *Opt Commun,* 119(1995)491.
17. Durnin J, Miceli (Jr) J J, Eberly J H, *Phys Rev Lett,* 58(1987)1499.
18. McLeod J H, *J Opt Soc Am*, 44(1954)592.
19. Wang H F, Gan F X, *Opt Engg,* 40(2001)851.
20. de Juana D M, Oti J E, Canales V F, Cagigal M P, *Opt Lett*, 28(2003)607.
21. Ledesma S, Campos J, Escalera J C, Yzuel M J, *Opt Lett,* 29(2004)932.
22. Escalera J C, Campos J, Yzuel M J, *Microwave Opt Technol Lett,* 7(1994)174.
23. Campos J, Escalera J C, Sheppard C J R, Yzuel M J, *J Mod Opt,* 47(2000)57.
24. Sales T R M, Morris G M, *J Opt Soc Am A*, 14(1997)1637.
25. Liu H, Yan Y, Yi D, Jin G, *Appl Opt,* 42(2003)1463.
26. Wang H, Gan F, *Appl Opt*, 40(2001)5658.
27. Cathey W T, Dowski E R, *Appl Opt*, 41(2002)6080.
28. Mezouari S, Harvey AR, *Opt Lett,* 28(2003)771.
29. Ledesma S, Escalera J C, Campos J, Yzuel M J, *Opt Commun*, 249(2005)183.
30. Sheppard C J R, Campos J, Escalera J C, Ledesma S, *Opt Commun*, 281(2008)913.
31. Sheppard C J R, Campos J, Escalera J C, Ledesma S, *Opt Commun*, 281(2008)3623.

32. Ledesma S, Campos J, Escalera J C, Yzuel M J, *Opt Exp*, 12(2004)2548.
33. Ledesma S, Campos J, Escalera J C, Yzuel M J, *Opt Comm,* 249(2005)183.
34. Sheppard C J R, *Opt Exp,* 21(2013)6339.
35. Wang H F, Sheppard C J R, Ravi K, Ho S T, Vienne G, *Laser Photonics Reviews*, 6(2012)354.
36. Chigrinov V G, Liquid crystal devices: physics and applications, (Artech House), 1999.
37. Campos J, Márquez A, Yzuel M J, Davis J A, Cottrell D M, Moreno I, *Appl Opt*, 39(2000)5965.
38. Gualdrón O, Davis J A, Nicolás J, Campos J, Yzuel M J, *Appl Opt*, 42(2003)1973.
39. Laude V, *Opt Commun*, 153(1998)134.
40. McOrist J, Sharma M D, Sheppard C J R, West E, Matsuda K, *Micron,* 34(2003)327.
41. Dou R, Giles M K, *Opt Lett*, 20(1995)1583.
42. Coufal H J, Psaltis D,Sincerbox B T, (eds), Holographic Data Storage, (Springer-Verlag, Berlin), 2000.
43. Davis J A, Escalera J C, Campos J, Márquez A, Yzuel M J, Iemmi C, *Opt Lett*, 24(1999)628.
44. Márquez A, Iemmi C, Escalera J C, Campos J, Ledesma S, Davis J A, Yzuel M J, *Appl Opt,* 40(2001)2316.
45. Campos J, Yzuel M J, Márquez A, Escalera J C, Davis J A, Iemmi C, Ledesma S, *Proceedings SPIE*, 4457(2001)99.
46. Hild R, Campos J, Yzuel M J, Iemmi C, Gimeno R, Escalera J C, *Proceedings SPIE*, 7000(2008)700018-1.
47. Hild R, Campos J, Yzuel M J, Iemmi C, Escalera J C, *Proceedings SPIE*, 7102(2008)7102R-1.
48. Márquez A, Iemmi C, Campos J, Escalera J C,Yzuel M J, *Opt Exp,* 13(2005)716.
49. Márquez A, Iemmi C, Campos J, Escalera J C,Yzuel M J, *Proceedings SPIE*, 6187(2006)61870E-1.
50. Campos J, Yzuel M J, *J Mod Opt*, 36(1989)733.
51. Tam E C, *Opt Lett*, 17(1992)369.
52. Takaki Y, Ohzu H, *Appl Opt*, 35(1996)6896.
53. Davis J A, Cottrell D M, Campos J, Yzuel M J, Moreno I, *Appl Opt*, 38(1999)5004.
54. Carcolé E, Campos J, Bosch S, *Appl Opt*, 33(1994)162.
55. Arrizón V, Carreón E, González L A, *Appl Opt*, 38(1999)5073.
56. Yzuel M J, Campos J, Márquez A, Escalera J C, Davis J A, Iemmi C, Ledesma S, *Appl Opt*, 39(2000)6034.
57. Dowski E (Jr), Cathey W T, *Appl Opt*, 34(1995)1859.
58. Gao X, Fee Z, Xu W, Gan F, *Appl Opt*, 44(2005)4870.
59. Born M, Wolf W, Principles of Optics, 6th edn (Pergamon Press, Oxford), 1985.
60. Gaskill D, Linear Systems, Fourier Transforms, and Optics, (John Wiley & Sons, Inc., New York), 1978.
61. Goodmann J W, Introduction to Fourier-Optics, 3rd Edn, (Roberts & Company, Greenwood Village), 2005.
62. Ben-Eliezer E, Zalevsky Z, Marom E, Konforti N, *J Opt A: Pure Appl Opt*, 5(2003)S164.
63. Ledesma S, Escalera J C, Campos J, Mazzaferri J, Yzuel M J, *Opt Commun*, 266(2006) 6.
64. Iemmi C, Campos J, Escalera J C, López-Coronado O, Gimeno R, Yzuel M J, *Opt Exp,*14(2006)10207.
65. Smith W J, Modern Optical Engineering, McGraw-Hill, 3rd Edn, (2000), pp. 402-412.
66. O'Shea D C, Suleski T J, Kathman A D, Prather D W, Diffractive Optics: Design, Fabrication, and Test, SPIE Press, Bellingham, (2004), Chapter 4.
67. Davis J A, Cottrell D M, Lilly R A, Connely S W, *Opt Lett*, 14(1989)420.
68. Carcolé E, Millán M S, Campos J, *Opt Lett*, 20(1995)2360.
69. Márquez A, Iemmi C, Campos J, Yzuel M J, *Opt Lett*, 31(2006)392.
70. Sheppard C J R, Ledesma S, Campos J, Escalera J C, *Opt Lett*, 32(2007)1713.
71. Sheppard C J R, *Opt Lett*, 32(2007)1653.
72. Yzuel M J, Escalera J C, Campos J, *J Mod Opt*, 36(1989)1341.
73. Ojeda-Castañeda J, Escalera J C, Yzuel M J, *Opt Commun*, 114(1994)189.
74. Airy G B, *Phil Mag Ser,* 3(1841)1.
75. Rayleigh L, *Monthly Notes of the Royal Astronomical Society,* 33(1872)59.

Juan Campos, Juan C Escalera, Andrés Márquez, and María J Yzuel

76. Welford W T, *J Opt Soc Am*, 50(1960)749.
77. Tschunko H F A, *Appl Opt*, 13(1974)1820.
78. Tschunko H F A, *Appl Opt*, 20(1981)168.
79. Thompson B J, *J Opt Soc Am*, 55(1965)145.
80. Osato K, Kino G S, Kubota S, *Opt Lett,* 18(1993)1244.
81. Sieracki C K, Hansen E W, *Proc SPIE*, 2184(1994)120.
82. Sheppard C J R, *Optik*, 99(1995)32.
83. de Juana D M, Canales V F, Valle P J, Cagigal M P, *Opt Commun,* 229(2004)71.
84. Cagigal M P, Oti J E, Canales V F, Valle P J, *Opt Commun*, 241(2004)249.
85. Luo H, Zhou C, *App Opt,* 43(2004)6242.
86. Jabbour T G, Kuebler S M, *Opt Exp,* 14(2005)1033.
87. Sheppard C J R, *Opt Lett*, 36(2011)1386.
88. Martinez-Corral M, Andrés P, Zapata-Rodriguez C J, Kowalczyk M, *Opt Commun*, 165(1999)267.
89. Martinez-Corral M, Ibañez-Lopez C, Saavedra G, *Opt Exp,*1(2003)1740.
90. Canales V F, Oti J E, Cagigal M P, *Opt Comm,* 247(2005)11.
91. Yun M, Liu L, Sun J, Liu D, *J Opt Soc Am A*, 22(2005)272.
92. Zhang Y, *Opt Comm,* 274(2007)37.
93. Hild R, Escalera J C, Yzuel M J, *Pure and Appl Opt*, 4(1995)795.
94. Hild R, Yzuel M J, Escalera J C, Campos J, *Opt Engg*, 37(1998)1353.
95. de Bougrenet de la Tocnaye J L, Dupont L, *Appl Opt*, 36(1997)1730.
96. Márquez A, Campos J, Yzuel M J, Moreno I, Davis J A, Iemmi C, Moreno A, Robert A, *Opt Engg*, 39(2000)3301.
97. Márquez A, Iemmi C, Moreno I, Davis J A, Campos J, Yzuel M J, *Opt Engg*, 40(2001)2558.
98. Nicolás J, Campos J,Yzuel M J, *J Opt Soc Am A*, 19(2002)1013.
99. Márquez A, Cazorla C, Yzuel M J, Campos J, *J Mod Opt*, 52(2005)633.
100. Soutar C, Lu K, *Opt Engg*, 33(1994)2704.
101. Davis J A, Allison D B, D'Nelly K G, Wilson M L, Moreno I, *Opt Engg*, 38(1999)705.
102. Davis J A, Tsai P, D'Nelly K G, Moreno I, *Opt Engg*, 38(1999)929.
103. Márquez A, Iemmi C, Moreno I, Campos J, Yzuel M J, *Opt Exp*, 13(2005)2111.